

General Disclaimer

One or more of the Following Statements may affect this Document

- This document has been reproduced from the best copy furnished by the organizational source. It is being released in the interest of making available as much information as possible.
- This document may contain data, which exceeds the sheet parameters. It was furnished in this condition by the organizational source and is the best copy available.
- This document may contain tone-on-tone or color graphs, charts and/or pictures, which have been reproduced in black and white.
- This document is paginated as submitted by the original source.
- Portions of this document are not fully legible due to the historical nature of some of the material. However, it is the best reproduction available from the original submission.

FINAL TECHNICAL REPORT

entitled

Atomic Oxygen Between 80 and 120 KM
Evidence for a Rapid Spatial Variation
in Vertical Transport Near the Ionosphere

(NASA-CR-155009) ATOMIC OXYGEN BETWEEN 80
AND 120 km: EVIDENCE FOR A RAPID SPATIAL
VARIATION IN VERTICAL TRANSPORT NEAR THE
IONOSPHERE Final Technical Report, Sep.
1976 - Aug. 1977 (Michigan Univ.) 46 p HC

N77-32660

HC A03/MFA01

Unclas

G3/46 47690

prepared under

NASA Grant NSG-7279

Title: Analysis of OGO-6 Photometer Data

Period: September 1976 - August 1977

by

Thomas M. Donahue
Barry Wasser

Department of Atmospheric and Oceanic Science
Space Physics Research Laboratory
The University of Michigan
Ann Arbor, Michigan 48109



ATOMIC OXYGEN BETWEEN 80 AND 120 KM: EVIDENCE FOR A RAPID
SPATIAL VARIATION IN VERTICAL TRANSPORT NEAR THE MESOPAUSE

Barry Wasser and T. M. Donahue

Department of Atmospheric and Oceanic Science
Space Physics Research Laboratory
The University of Michigan
Ann Arbor, Michigan 48109

ABSTRACT

Analysis of OGO-6 OI Green Line photometer results has been carried out for 8 cases when the alignment of the spacecraft was such that local emission rates could be determined below the altitude of maximum emission and down to about 80 km. The results show a variation on a scale of $6^\circ - 8^\circ$ in latitude between regions where the emission rate increases rapidly between 90 and 95 km and regions where it increases slowly from 80 km to 95 km. Latitude-altitude maps of iso-emissivity contours and iso-density contours for [O] are presented. The latter are computed under three assumptions concerning excitation mechanisms. Comparisons of the spatial variations of oxygen density with the results of a time dependent theory suggest the regions of strong downward transport alternate on a scale of about 1000 km with regions of weak transport near 90 km. In the first case conversion of O to O_3 at night appears to be overwhelmed by downward transport of O.

INTRODUCTION

Slant column emission rates from the atomic oxygen green airglow at 557.7 nm were measured by the horizon scanning photometer flown on OGO-6. Reports of results obtained from the analysis of these observations have been published in a series of papers [Thomas and Donahue, 1972; Donahue et al., 1973, 1974; Donahue, 1975; Donahue and Carignan, 1975]. A detailed description of the instrument and its operation can be found in Donahue et al. [1973]. The photometer was equipped with a stepping mirror so that it could scan the horizon in 128 steps of 7.5' from 10° to 26° below the local horizontal and had an angular field of view of 7.5' in the vertical and 4.2° horizontally. The satellite orbit had a perigee of 397 km and an apogee of 1098 km and an inclination of 82°. From perigee the field of view of the photometer encompassed a vertical surface less than 5 km in extent 100 km above the earth's surface.

The green airglow features normally detected by the photometer were an F_1 region glow at tropical latitudes associated with the electron recombination of O_2^+ [Thomas and Donahue, 1972] and the well known airglow layer in the lower thermosphere generally assumed to be associated with the recombination of atomic oxygen. The excitation mechanisms proposed for this airglow are usually associated with the names of Chapman [1931], Barth [1964], Slanger and Black [1977]



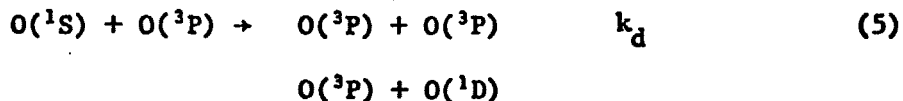
or



followed after 0.75 seconds by



Alternatively, $\text{O}(^1\text{S})$ can be quenched by two processes



or



In the early analysis of the photometer data [Donahue et al., 1973] slant emission rates were converted to local volume emission rates by a simple inversion which was based on the assumption that the emission rates at a given altitude were independent of latitude. This assumption was known to be incorrect, for the results of the analyses themselves demonstrated large variations in the emission rates with latitude. It was characteristic of the observations that fluctuations of the order of 50 to 100% occurred on a latitude scale of tens of degrees superimposed on systematic patterns hemispherical in scale. The "uniform layer" assumption nevertheless is a reasonable approximation to use in deriving local emission rates from the integrated slant rates for the region above the altitude of maximum emission because the overwhelming contribution to the slant emission there comes from a short horizontal region near the lowest altitude attained along the line of sight. For fields of view that pass below the maximum, however, there are large contributions to the

slant intensity from regions closer to and further from the satellite than the lowest altitude along the line of sight. This situation becomes more and more serious as the altitude probed decreases since the volume emission rate decreases with altitude. There is no way to correct for this effect as long as the field of view lies in a plane that makes a large angle with the orbital plane. However, there were occasions when the satellite yawed in such a way that the field of view lay near the orbital plane long enough for a large number of vertical scan of the photometer's stepping mirror to be obtained. Under these circumstances, it is possible to use a technique developed by Thomas and Donahue [1972] to obtain reliable estimates of the emission rates at altitudes below the location of the maximum emitting region. The reason is that each vertical scan occurs rapidly enough that a given point in space is sampled many times along varying lines of sight as the satellite moves in its orbit (Figure 1). Figures 1 and 2 in the paper by Thomas and Donahue [1972] are useful in producing a visualization of this effect.

The latitude spacing between scans such as 1 and 2 or 3 and 4 (Figure 1) is about 3.3° at low latitudes and between scans 2 and 3 is only 1.1° . This pattern is the consequence of the fact that pairs of scans were performed with a green and a yellow (589 nm) filter alternately in the photometer.

DATA ANALYSIS

To calculate the local volume emission rates from the data obtained, the region studied by a sequence of vertical photometer scans is divided into a matrix whose dimensions are 1 km in altitude by 0.5° in latitude. In the case of each vertical scan, the local volume emission rates are calculated for a sequence of matrix elements at the latitude where the line of sight along which the slant emission rate is a maximum passes closest to the earth's surface. These calculations are made using the uniform layer assumption. Next, the elements in each row (latitude) and column (altitude) containing an element with a "measured" emission rate are assigned rates determined by linear interpolation between pairs of "measured" emitting elements. All other elements are assigned an emission rate of $1 \text{ cm}^{-3} \text{ s}^{-1}$. This is the first order approximation to the emission rate matrix.

Next, the calculated slant emission rates from the first order matrix are determined from the sum over all elements along the lines of sight corresponding to given mirror positions. If the calculated values differ from the observed ones, the emitting elements involved in each of such sums are corrected by multiplying each of them by the ratio of the observed to the calculated slant emission rate for the mirror position involved. (Some of the unit matrix elements will be involved in this procedure. Their values will then be the ratio of observed to calculated slant emission rates.) This procedure is followed for each scan of the photometer mirror. Where an emission rate matrix element already traversed by a previous scan is encountered in a subsequent scan it is omitted from the summation and correction process in the latter scan. A second approximation to the emission matrix is thus obtained. This matrix is then smoothed by taking a running average in the vertical (involving three adjacent elements) and in the horizontal (using five adjacent elements). During this smoothing process a large number of the elements in

the matrix will be assigned values differing from unity. Next, the slant emission rates from the smoothed matrix are calculated, compared to the observed emission rates, corrected and smoothed. This procedure is normally repeated 25 times and the result used to plot iso-emission rate maps such as shown in Figures 2a and 9a. In the case of pass 2269 on day 313 (Figures 8a and 10) the adequacy of the iteration procedure was calculated by iterating 300 times instead of 25 times. While some structure in the coarser map of Figure 8a disappeared from Figure 10 as a result of 12 times as many iterations, the improvement is not great enough to warrant the 12 fold increase in computer time involved.

RESULTS

The emission rate maps in Figures 2a-9a are for the following orbit segments:

Day 304, pass 2135 from -26.6° to -7.1° latitude

304, pass 2142 from -20.1° to -4.8° latitude

311, pass 2238 from 19.2° to 33.6°

311, pass 2239 from 15.5° to 24.3°

311, pass 2243 from 14.2° to 20.5°

311, pass 2244 from 8.8° to 22.4°

311, pass 2269 from 18.6° to 27.8°

329, pass 2505 from 48.8° to 54.1°

From the emission rates the atomic oxygen density profiles may be calculated provided all relevant rate constants are known and the excitation of $O(^1S)$ occurs as postulated. Unfortunately, there is still some uncertainty with regard to the values for the rate constants k_a , k_b , k_c , k_d , and k_e . Donahue et al. [1973] in analyzing their data made various assumptions with regard to the values of rate constants k_a , k_d , and k_e . One of these was that these rate constants have the following values.

$$k_a = 4.8 \times 10^{-33} \text{ cm}^6 \text{ s}^{-1}$$

$$k_d = 1.2 \times 10^{-11} \exp(-226/T) \text{ cm}^3 \text{ s}^{-1}$$

$$k_e = 4.3 \times 10^{-12} \exp(-853/T) \text{ cm}^3 \text{ s}^{-1}$$

where k_d and k_e are taken from Slanger and Black [1973] and k_a from Felder and Young [1972]. Recently, as a result of analyzing data obtained from an experiment in which photometer and mass spectrometer observations obtained by Atmosphere Explorer (AE-C) were coordinated with a vertical profile for the green line emission rate obtained from a sounding rocket [Wasser et al., 1976] deduced a rate constant for k_a given by

$$k_a = 2.4 \times 10^{-36} \exp(1000/T) \text{ cm}^3 \text{ s}^{-1}$$

Recently, Slanger and Black [1977] have argued from laboratory measurements and analyses of satellite and rocket data that the Barth mechanism can account for the airglow. According to their mechanism

$$[O] = \left\{ \frac{E}{K [M]} (1 + \tau_R k_d [O] + \tau_R k_e [O_2]) \cdot \left(\frac{K}{yzk_{36}} [O] + [M] + \frac{1}{\tau_R k_f} \right) \right\}^{1/3} \quad (7)$$

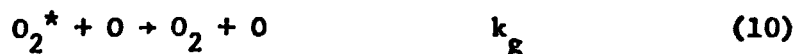
where

$$K = k_b k_c / k_f$$

$$y = k_b / k_{36}$$

$$z = k_c / k_g$$

and



The emission rates have been converted to oxygen density profiles for each of these three sets of assumptions. The cases will be labelled C_1 , C_2 , and SB. The iso-density contours corresponding to the eight emission rate maps are plotted in Figures 2b, c, d-9b, c, d. Vertical cuts through the emission rate and density maps at selected latitude are shown in Figures 11-19. The generally smaller value of the Chapman rate constant for Case C_2 than for C_1 and its decreasing value with T causes the C_2 densities to be larger than C_1

by a factor of about 2 near 95 km and the ratio of C_2 to C_1 densities to increase with altitude as T increases. At 120 km, the ratio is typically 5. Thus, C_2 gives larger values for $[O]$ than C_1 and a slower decrease with altitude. The SB densities are typically smaller than or of the order of C_1 densities near 90 km but rise much more rapidly than C_1 densities so that the ratio increases from less than 1 to a value of 2 to 3 at about 102 km. Thereafter the ratio of SB to C_1 densities decreases very slowly or remains relatively constant to 120 km at a value in the neighborhood of 2. The low densities for a given prediction by the SB mechanism near 80 km and the increase with altitude relative to C_1 is a consequence of the increasing rate for Reaction (2) as $[M]$ increases. In fact it is easy to show that

$$\frac{[O]_{SB}}{[O]_{C_1}} = \left\{ \frac{k_a}{K [M]} \right\}^{1/3} \left\{ \frac{K}{yzk_{36}} [O] + [M] + (\tau_R' k_f)^{-1} \right\}^{1/3} \quad (11)$$

Not all of the emission rates obtained by this method are physically meaningful. One important property of the photometer detector is that it was designed to produce an output voltage that stepped in intervals equivalent to 10R. Thus a reading of zero meant that the emission in the field of view was less than 5R. The first step in output voltage above zero indicated an emission rate between 5 and 15R, the second step 15 and 25R and so on. Furthermore, it is necessary to extrapolate a background counting rate from data obtained when the field of view was above 120 km and subtract this background from the slant rate measured at low altitudes. The uncertainty introduced by background subtraction between 90 and 80 km can hardly be less than 20R except in the very best of circumstances. It can never be less than 5R. At high altitude the emission rate decreased with a scale height typically of about 3 km. Hence the Chapman function is about 115 and the minimum detectable emission rate is about $0.15 \text{ cm}^{-3} \text{ s}^{-1}$. This limit is marked on all of the emission rate maps and is

reflected in the iso-density profile maps for [O] as well. Another way of formulating the criterion for a minimum detectable emission rate makes use of the fact that the photometer's field extends 5 km in the vertical near 90 km. Hence, unless the emission rate averaged over 5 km is above a certain minimum value it cannot contribute significantly to the observed slant emission rate. That is to say that a condition that must be assigned is

$$2\sqrt{2Rd} \overline{E}_m = 4\pi I_m$$

where d is 5 km, R is the radius of the earth plus 90 km and $4\pi I_m$ is the minimum detectable slant emission rate near 90 km. If the minimum detectable signal is, say 25R, because of uncertainty in the background subtraction

$$\overline{E}_m = 0.5 \text{ cm}^{-3} \text{ s}^{-1}$$

A glance at the emission rate maps is enough to demonstrate that there is a large amount of structure in the emission, both in altitude and latitude. The altitude of maximum emission varies with latitude but stays usually between 95 km and 100 km. Most striking is the variation in latitude of the vertical gradient in emission rate. Regions in which the emission rate increases rapidly with altitude near 90 km alternate with regions of much slower variation. The latitude difference between regions of rapidly varying emission rates and slowly varying rates is 6° to 7°. In most cases where the emission changes slowly, the emission rate deduced at 80 km is still significantly large by any criterion. In Figures 11a-18a we show the results of an error analysis of the calculated emission rates in addition to indicating on the graphs minimum observationally meaningful levels of emission rates: 0.15 and 0.5 $\text{cm}^{-3} \text{ s}^{-1}$. It can be seen that in the regions of steep gradients

the emission rates increase rapidly near 90 km from values less than $0.5 \text{ cm}^{-3} \text{ s}^{-1}$ to maximums near 97 km of the order of 20 to $100 \text{ cm}^{-3} \text{ s}^{-1}$. On the other hand, at the latitudes where the emission rate varies slowly it often is in the range of 5 to $10 \text{ cm}^{-3} \text{ s}^{-1}$ at 80 km. Furthermore, the calculated values in these latter cases are usually physically significant according to the results of the error analysis. Pass 2269 (Figure 17) is particularly interesting in this regard. (This is the case in which 300 iterations were performed.) In Figure 17a the emission rate profiles at 16.6° and 28° vary slowly from about 6 to $7 \text{ cm}^{-3} \text{ s}^{-1}$ at 80 km to about $40 \text{ cm}^{-3} \text{ s}^{-1}$ between 95 and 100 km. On the other hand, at 18.6° and 23.6° the emission rates calculated at 88 km and below are mostly in the range 10^{-2} to $10^{-1} \text{ cm}^{-3} \text{ s}^{-1}$, far too small to be meaningful. By 90 km, they jump to about $5 \text{ cm}^{-3} \text{ s}^{-1}$.

DISCUSSION

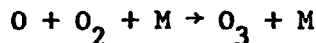
The variation in the oxygen density with altitude and latitude will resemble the emission rate variation, the exact values being determined by the mechanism selected for the green line excitation. The data for pass 2269 between 13° and 28° were obtained at a local time of 24^h40^m. In Figures 17b, c, and d we show the densities at the 4 selected latitudes obtained following the analysis of Donahue et al. [1973]. For comparison we also show the results of a calculation by S. C. Liu [private communication, 1977] using a time-dependent one-dimensional coupled flow model for atomic oxygen at local midnight and at 1600 hours. The time dependent equations that determine the behavior of odd oxygen between 80 and 120 km are the following:

$$\begin{aligned} \frac{\partial [O_x]}{\partial t} + \frac{\partial \phi(O_x)}{\partial z} = & -[O] \{ k_{17}[OH] + k_{20}[HO_2] + k_{28}[NO_2] \\ & + 2 k_{36}[O][M] + 2 k_{35}[O_3] \} - [O_3] \{ k_{14}[H] + k_{19}[OH] \\ & + k_{21}[HO_2] \} + 2 J_1[O_2] \end{aligned} \quad (12)$$

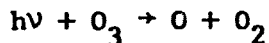
$$\begin{aligned} \frac{\partial [O_3]}{\partial t} + \frac{\partial \phi(O_3)}{\partial z} = & k_{34}[O][O_2][M] - [O_3] \{ k_{14}[H] + k_{35}[O] \\ & + k_{19}[OH] \} - J_2[O_3] \end{aligned} \quad (13)$$

$$\frac{\partial [O]}{\partial t} + \frac{\partial \phi(O)}{\partial z} = -[O] \{ k_{34}[O_2][M] + 2 k_{36}[O][M] \} + J_2[O_3] + 2 J_1[O_2] \quad (14)$$

where the rate constants k_1 are defined in the paper by Liu et al. [1976] and the values used for these rate constants are those recommended by Hampson et al. [1977] and Margitan [1977]. In this model, the solar zenith angle at noon was 25°. The eddy diffusion coefficient above 80 km was held at $5.6 \times 10^5 \text{ cm}^2 \text{ s}^{-1}$. The large diurnal variation in atomic oxygen below 90 km is caused by the fact that the conversion of O to O_3 by three body recombination



is not compensated for by photolysis



(The effect of O_2 photolysis at these altitudes is relatively insignificant). However, because of the non-negligible value for the eddy diffusion coefficient there is a strong downward flow of atomic oxygen below 90 km that causes the oxygen densities to be larger at any given altitude than the value that would prevail if photochemistry alone had determined the densities. Chemical loss rates for O, O_3 and O_x as well as production rates are shown in Tables 1a and 1b. These are gross rates to be used in a continuity equation

$$-\text{div } \phi = p - l$$

where ϕ is the oxygen flux, p the rate of O production and l the rate of O loss.

Table 1a. Gross Production per cm^3 per day

Altitude	O_x	O_3	O
110 km	1.71×10^{10}	1.05×10^7	1.71×10^{10}
110	2.10×10^{10}	1.64×10^9	2.01×10^{10}
90	5.54×10^{10}	3.27×10^{10}	4.19×10^{10}
80	1.00×10^{11}	3.76×10^{10}	6.89×10^{10}
70	2.79×10^{11}	1.67×10^{11}	1.15×10^{10}

Table 1b. Gross Loss per cm^3 per day

Altitude	O_x	O_3	O
110 km	1.74×10^8	1.04×10^7	1.69×10^8
100	1.01×10^{10}	1.64×10^9	9.31×10^9
90	6.96×10^{10}	3.27×10^{10}	5.61×10^{10}
80	1.06×10^{11}	3.90×10^{10}	7.58×10^{10}
70	2.78×10^{11}	1.67×10^{11}	1.15×10^{11}

It is very interesting that a characteristic of the derived densities in the latitude regimes of steep gradients is that they increase more rapidly with altitude between 85 and 90 km than the values computed from the coupled flow-chemical theory and much more slowly in the other regimes. This suggests that the effectiveness of downward transport varies strongly with latitude. At 18.6° and 23.6° on pass 2269 there appears to be weak downward transport of oxygen below 95 km. The midnight oxygen densities correspond to photochemical values. On the other hand at 16.6° and 28° during that orbit the downward transport is strong enough to cause midnight oxygen densities at 80 km orders of magnitude

larger than those expected from the time dependent coupled flow model and even about 4 times as large as the daytime values predicted by theory. The simplest explanation we can find for these results is that downward transport in the neighborhood of the mesopause varies on a 6° latitude scale from very weak to very strong.

One might have expected to find a reflection of this pattern in the magnitude of the maximum O density. Where transport is strong, the maximum density should be relatively small. This expectation is disappointed. However, there is no reason to believe that a given flow condition is constant with altitude or that it is confined to a vertical surface. It may well vary with altitude, latitude and time. It is probably significant that the structure in the slant emission rate as a function of altitude [Donahue et al., 1973] shows a variation on a scale of the order of 15° , as does the bottom side structure reported here.

In Figures 18 and 19 we show the results obtained on one interesting pass, 2505, on day 329 relatively early in the evening (2120 hours) and at high latitude. The very slow altitude variation between 80 and 104 km at 53.8° latitude is not characteristic of results obtained in any other case studied.

A comprehensive summary of the maximum atomic oxygen densities (for case C_1) for day 304 and 311, as well as others, was presented by Donahue et al. [1974]. These data are given in the form of iso-density contour maps. The nature of these maps indicates very large variability both temporally and spatially. Orbits which appear to overlap latitude regimes in this work, encompass regions which can be quite different as is seen in the patchy structure of the maximum atomic oxygen densities presented in the earlier paper. In the case of day 304 orbit 2142 generally has larger densities than orbit 2135 but is separated by about 180° of longitude and about 11 hours GMT. For the situation on day 311 of orbit 2238 and 2239 little change had taken place (see Donahue et al. [1974]) and the maps shown in Figure 4 and 5 are

very similar in structure and magnitude. A dramatic example is the closed contour of about 4.8×10^{10} atoms/cm³ occurring at 20° latitude and 110 km in both Figures 4a and 5a. The consecutive orbits 2243 and 2244, however, Donahue et al. [1974] showed a very definite transition in densities. This can be seen in Figures 6 and 7 as decreased densities at all altitudes above 97 km from orbit 2243 to 2244. The temporal variation cannot be resolved from the spatial in this analysis, but used in conjunction with the previous works (Donahue et al. [1973, 1974]) provide a good survey of the four dimensional variations of atomic oxygen.

Acknowledgements. This work was supported in part by NASA under Grant NSG-7279 and the Atmospheric Research Section of the National Science Foundation. We wish to thank Dr. Shaw Chen Liu for providing invaluable information and insights.

References

- Barth, C., Three-body reactions, Ann. de Géophys., 20, 182, 1964.
- Chapman, S., Some phenomena of the upper atmosphere, Proc. Roy. Soc. London, A132, 353, 1931.
- Donahue, T. M., OGO-6 observations of 5577A, in Atmosphere of Earth and the Planets, ed. B. M. McCormac, D. Reidel Publishing Co., Dordrecht, Netherlands 289 p., 1975.
- Donahue, T. M., B. Guenther, and R. J. Thomas, Distribution of atomic oxygen in the upper atmosphere deduced from OGO-6 airglow observations, J. Geophys. Res., 78, 6662, 1973.
- Donahue, T. M., B. Guenther and R. J. Thomas, Spatial and temporal behavior of atomic oxygen determined by OGO-6 airglow observations, J. Geophys. Res., 79, 1959, 1974. ,
- Donahue, T. M., and G. R. Carignan, The temperature gradient between 100 and 120 km, J. Geophys. Res., 80, 4565, 1975.
- Felder, W., and R. A. Young, Quenching of $O(^1S)$ by $O(^3P)$, J. Chem. Phys., 56, 6028, 1972.
- Hampson, R. F., D. Garvin, M. J. Kurjlo, R. E. Huie and W. Tsang, Rate constants for NO_x reactions and those of $O(^1D)$, position paper for NASA CFM Assessment, 1977.
- Liu, S. C., T. M. Donahue, R. J. Cicerone and W. L. Chameides, Effect of water vapor on the destruction of ozone in the stratosphere perturbed by ClX or NO_x pollutants, J. Geophys. Res., 81, 3111, 1976.
- Margitan, J. J., HO_x reaction rates, position paper for NASA CFM Assessment, 1977.
- Slinger, T. G., and G. Black, $O(^1S)$ quenching profile between 75 and 115 km, Planet. Space Sci., 21, 1757, 1973.

Slinger, T. G., and G. Black, O(¹S) in the lower thermosphere - Chapman vs. Barth,
Planet. Space Sci., 77, 79, 1977.

Thomas, R. J., and T. M. Donahue, Analysis of OGO-6 observations of the OI 5577Å
tropical nightglow, J. Geophys. Res., 77, 3557, 1972.

Wasser, B., D. W. Rusch, W. E. Sharp, P. B. Hays, G. R. Carignan, Evidence for
the source of the mesopause OI(5577Å) emission, EOS Trans. Amer. Geophys.
Union., 57, 967, 1976.

Figure Captions

Figure 1. Geometry of the airglow observations. The outermost circle represents the satellite orbit, the next the green airglow emission maximum and the third the earth's surface. The line of sight of the photometer for selected scanning mirror positions is indicated at four successive positions of the satellite at which the green line is being observed.

Figure 2a. Iso-emission rate contours in photons $\text{cm}^{-3}\text{s}^{-1}$ obtained during orbit 2135 of OGO-6 on day 304, 1969. The heavy line at the top of the figure defines the transition to a region where the emission rate is lower than $0.15 \text{ cm}^{-3}\text{s}^{-1}$ and the heavy line at the bottom the altitude at which the average emission rate becomes less than $0.5 \text{ cm}^{-3}\text{s}^{-1}$.

Figure 2b. (C_1) Contours of constant oxygen density on orbit 2135 in units of 10^{10}cm^{-3} calculated according to the version of the Chapman mechanism used by Donahue et al. [1973]. Heavy lines separate regions where the densities are calculated from meaningful and non-significant emission rates.

Figure 2c. (C_2) Contours of constant oxygen density on orbit 2135 in units of 10^{10}cm^{-3} calculated according to the version of the Chapman mechanism developed by Wasser et al. [1976]. Heavy lines separate regions where the densities are calculated from meaningful and non-significant emission rates.

Figure 2d. (SB) Contours of constant oxygen density on orbit 2135 in units of 10^{10}cm^{-3} calculated according to the version of the Barth mechanism developed by Slanger and Black [1977]. Heavy lines separate regions where the densities are calculated from meaningful and non-significant emission rates.

Figure 3a. See Figure 2a, iso-emission rate contours in units of photons $\text{cm}^{-3}\text{s}^{-1}$, orbit 2142, day 304, 1969.

Figure 3b. (C_1) See Figure 2b, iso-density contours in units of 10^{10}cm^{-3} , orbit 2142, day 304, 1969, Chapman mechanism [Donahue et al., 1973].

Figure 3c. (C_2) See Figure 2c, iso-density contours in units of 10^{10}cm^{-3} , orbit 2142, day 304, 1969, Chapman mechanism [Wasser et al., 1976].

Figure 3d. (SB) See Figure 2d, iso-density contours in units of 10^{10}cm^{-3} , orbit 2142, day 304, 1969, Barth mechanism [Slanger and Black, 1977].

Figure 4a. See Figure 2a, iso-emission rate contours in units of photons $\text{cm}^{-3}\text{s}^{-1}$, orbit 2238, day 311, 1969.

Figure 4b. (C_1) See Figure 2b, iso-density contours in units of 10^{10}cm^{-3} , orbit 2238, day 311, 1969, Chapman mechanism [Donahue et al., 1973].

Figure 4c. (C_2) See Figure 2c, iso-density contours in units of 10^{10}cm^{-3} , orbit 2238, day 311, 1969, Chapman mechanism, [Wasser et al., 1976].

Figure 4d. (SB) See Figure 2d, iso-density contours in units of 10^{10}cm^{-3} , orbit 2238, day 311, 1969, Barth mechanism [Slanger and Black, 1977].

Figure 5a. See Figure 2a, iso-emission rate contours in units of photons $\text{cm}^{-3}\text{s}^{-1}$, orbit 2239, day 311, 1969.

Figure 5b. (C_1) See Figure 2b, iso-emission contours in units of 10^{10}cm^{-3} , orbit 2239, day 311, 1969, Chapman mechanism [Donahue et al., 1973].

Figure 5c. (C_2) See Figure 2c, iso-density contours in units of 10^{10}cm^{-3} , orbit 2239, day 311, 1969, Chapman mechanism [Wasser et al., 1976].

Figure 5d. (SB) See Figure 2d, iso-density contours in units of 10^{10}cm^{-3} , orbit 2239, day 311, 1969, Barth mechanism [Slanger and Black, 1977].

Figure 6a. See Figure 2a, iso-emission rate contours in units of photons $\text{cm}^{-3}\text{s}^{-1}$, orbit 2243, day 311, 1969.

Figure 6b. (C_1) See Figure 2b, iso-density contours in units of 10^{10}cm^{-3} , orbit 2243, day 311, 1969, Chapman mechanism [Donahue et al., 1973].

Figure 6c. (C_2) See Figure 2c, iso-density contours in units of 10^{10}cm^{-3} , orbit 2243, day 311, 1969, Chapman mechanism [Wasser et al., 1976].

Figure 6d. (SB) See Figure 2d, iso-density contours in units of 10^{10}cm^{-3} , orbit 2243, day 311, 1969, Barth mechanism [Slanger and Black, 1977].

Figure 7a. See Figure 2a, iso-emission rate contours in units of photons $\text{cm}^{-3}\text{s}^{-1}$, orbit 2244, day 311, 1969.

Figure 7b. (C_1) See Figure 2b, iso-density contours in units of 10^{10}cm^{-3} , orbit 2244, day 311, 1969, Chapman mechanism [Donahue et al., 1973].

Figure 7c. (C_2) See Figure 2c, iso-density contours in units of 10^{10}cm^{-3} , orbit 2244, day 311, 1969, Chapman mechanism [Wasser et al., 1976].

Figure 7d. (SB) See Figure 2d, iso-density contours in units of 10^{10}cm^{-3} , orbit 2244, day 311, 1969, Barth mechanism [Slanger and Black, 1977].

Figure 8a. See Figure 2a, iso-emission contours in units of photons $\text{cm}^{-3}\text{s}^{-1}$, orbit 2269, day 311, 1969.

Figure 8b. (C_1) See Figure 2b, iso-density contours in units of 10^{10}cm^{-3} , orbit 2269, day 311, 1969, Chapman mechanism [Donahue et al., 1973].

Figure 8c. (C_2) See Figure 2c, iso-density contours in units of 10^{10}cm^{-3} , orbit 2269, day 311, 1969, Chapman mechanism [Wasser et al., 1976].

Figure 8d. (SB) See Figure 2d, iso-density contours in units of 10^{10}cm^{-3} , orbit 2269, day 311, 1969, Barth mechanism [Slanger and Black, 1977].

Figure 9a. See Figure 2a, iso-emission contours in units of photons $\text{cm}^{-3}\text{s}^{-1}$, orbit 2505, day 329, 1969.

Figure 9b. (C_1) See Figure 2b, iso-density contours in units of 10^{10}cm^{-3} , orbit 2505, day 329, 1969, Chapman mechanism [Donahue et al., 1973].

Figure 9c. (C_2) See Figure 2c, iso-density contours in units of 10^{10}cm^{-3} , orbit 2505, day 329, 1969, Chapman mechanism [Wasser et al., 1976].

Figure 9d. (SB) See Figure 2d, iso-density contours in units of 10^{10}cm^{-3} , orbit 2505, day 329, 1969, Barth mechanism [Slanger and Black, 1977].

Figure 10. Emission rates in photons $\text{cm}^{-3}\text{s}^{-1}$ for the same data as Figure 8a except that 300 iterations were performed in arriving at this emission matrix instead of 25 as in Figure 8a.

Figure 11a. 557.7 nm volume emission rate in photons $\text{cm}^{-3}\text{s}^{-1}$ as a function of altitude at selected latitudes of orbit 2135, day 304, 1969. Minimum detectable emission rates of $0.15 \text{ cm}^{-3}\text{s}^{-1}$ and $0.5 \text{ cm}^{-3}\text{s}^{-1}$ are indicated by vertical lines. Error bars are assigned to calculated values at -26.6° latitude (triangles).

Figure 11b. (C_1) Oxygen densities calculated from the emission rates of Figure 11a following the Chapman mechanism according to Donahue et al. [1973]. Minimum meaningful densities corresponding to the minimum detectable emission rates of Figure 11a are indicated by vertical lines.

Figure 11c. (C_2) Oxygen densities calculated from the emission rates of Figure 11a following the Chapman mechanism according to Wasser et al. [1976]. Minimum meaningful densities corresponding to the minimum detectable emission rates of Figure 11a are indicated by vertical lines.

Figure 11d. (SB) Oxygen densities calculated from the emission rates of Figure 11a following the Barth mechanism according to Slanger and Black [1977]. Minimum meaningful densities corresponding to the minimum detectable emission rates of Figure 11a are indicated by vertical lines.

Figure 12a. See Figure 11a, orbit 2142, day 304, 1969.

Figure 12b. (C_1) See Figure 11b, orbit 2142, day 304, 1969, Chapman mechanism, [Donahue et al., 1973].

Figure 12c. (C_2) See Figure 11c, orbit 2142, day 304, 1969, Chapman mechanism, [Wasser et al., 1976].

Figure 12d. (SB) See Figure 11d, orbit 2142, day 305, 1969, Barth mechanism,
[Slanger and Black, 1977].

Figure 13a. See Figure 11a, orbit 2238, day 311, 1969.

Figure 13b. (C_1) See Figure 11b, orbit 2238, day 311, 1969, Chapman mechanism,
[Donahue et al., 1973].

Figure 13c. (C_2) See Figure 11c, orbit 2238, day 311, 1969, Chapman mechanism,
[Wasser et al., 1976].

Figure 13d. (SB) See Figure 11d, orbit 2238, day 311, 1969, Barth mechanism,
[Slanger and Black, 1977].

Figure 14a. See Figure 11a, orbit 2239, day 311, 1969.

Figure 14b. (C_1) See Figure 11b, orbit 2239, day 311, 1969, Chapman mechanism,
[Donahue et al., 1973].

Figure 14c. (C_2) See Figure 11c, orbit 2239, day 311, 1969, Chapman mechanism,
[Wasser et al., 1976].

Figure 14d. (SB) See Figure 11d, orbit 2239, day 311, 1969, Barth mechanism,
[Slanger and Black, 1977].

Figure 15a. See Figure 11a, orbit 2243, day 311, 1969.

Figure 15b. (C_1) See Figure 11b, orbit 2243, day 311, 1969, Chapman mechanism,
[Donahue et al., 1973].

Figure 15c. (C_2) See Figure 11c, orbit 2243, day 311, 1969, Chapman mechanism, [Wasser et al., 1976].

Figure 15d. (SB) See Figure 11d, orbit 2243, day 311, 1969, Barth mechanism, [Slanger and Black, 1977].

Figure 16a. See Figure 11a, orbit 2244, day 311, 1969.

Figure 16b. (C_1) See Figure 11b, orbit 2244, day 311, 1969, Chapman mechanism, [Donahue et al., 1973].

Figure 16c. (C_2) See Figure 11c, orbit 2244, day 311, 1969, Chapman mechanism, [Wasser et al., 1976].

Figure 16d. (SB) See Figure 11d, orbit 2244, day 311, 1969, Barth mechanism, [Slanger and Black, 1977].

Figure 17a. See Figure 11a, orbit 2269, day 311, 1969.

Figure 17b. (C_1) See Figure 11b, orbit 2269, day 311, 1969, Chapman mechanism, [Donahue et al., 1973]. Model densities are shown for 1600 hours and 2400 hours.

Figure 17c. (C_2) See Figure 11c, orbit 2269, day 311, 1969, Chapman mechanism, [Wasser et al., 1976]. Model densities are shown for 1600 hours and 2400 hours.

Figure 17d. (SB) See Figure 11d, orbit 2269, day 311, 1969, Barth mechanism, [Slanger and Black, 1977]. Model densities are shown for 1600 hours and 2400 hours.

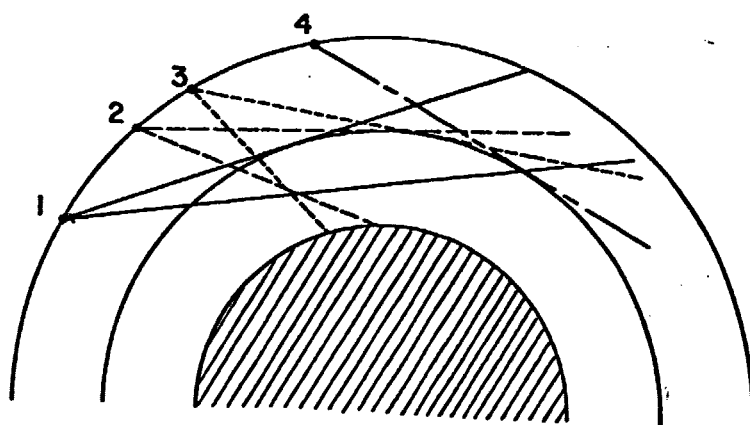
Figure 18a. See Figure 11a, orbit 2505, day 329, 1969.

Figure 18b. (C_1) See Figure 11b, orbit 2505, day 329, 1969, Chapman mechanism,
[Donahue et al., 1973].

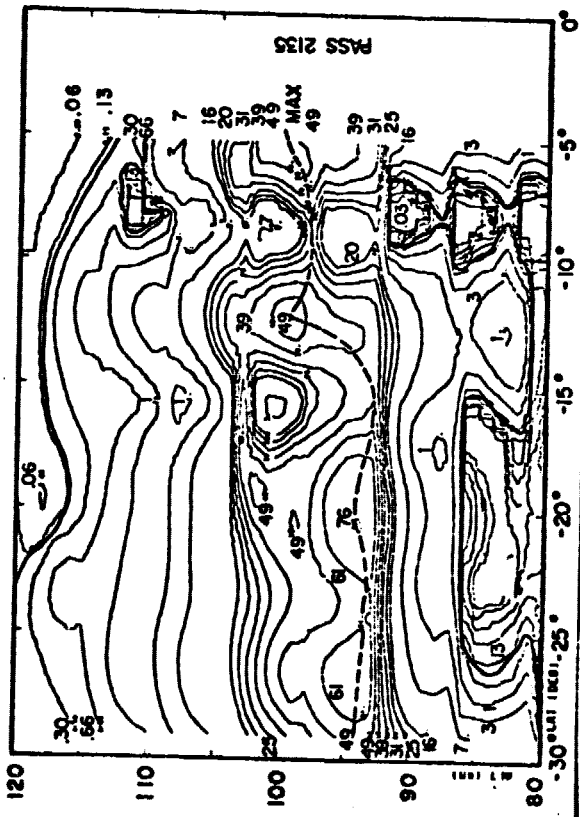
Figure 18c. (C_2) See Figure 11c, orbit 2505, day 329, 1969, Chapman mechanism,
[Wasser et al., 1976].

Figure 18d. (SB) See Figure 11d, orbit 2505, day 329, 1969, Barth mechanism,
[Slanger and Black, 1977].

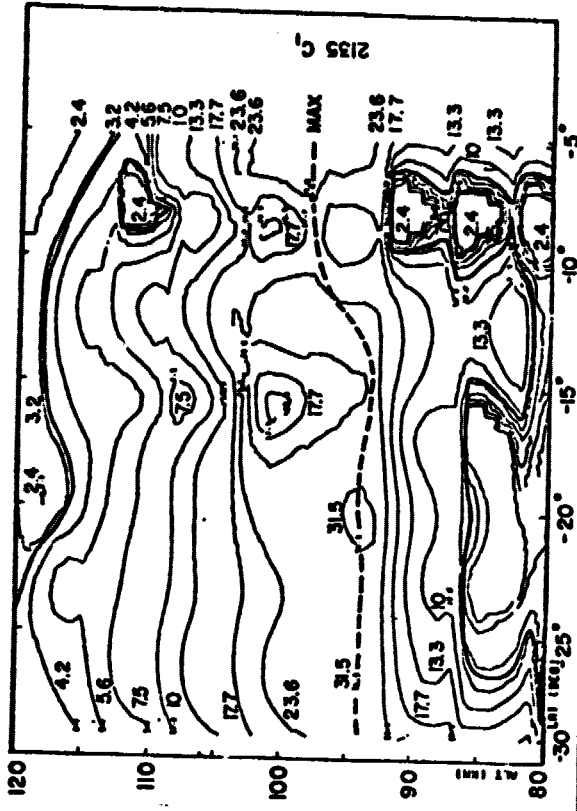
Figure 19. Oxygen densities of Figure 18b compared to calculated values at 12^h00
16^h00 and 20^h00.



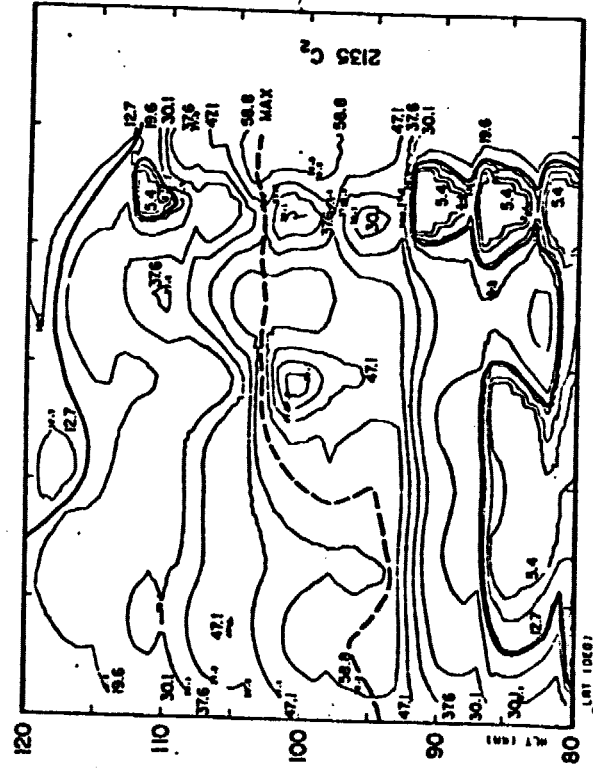
1

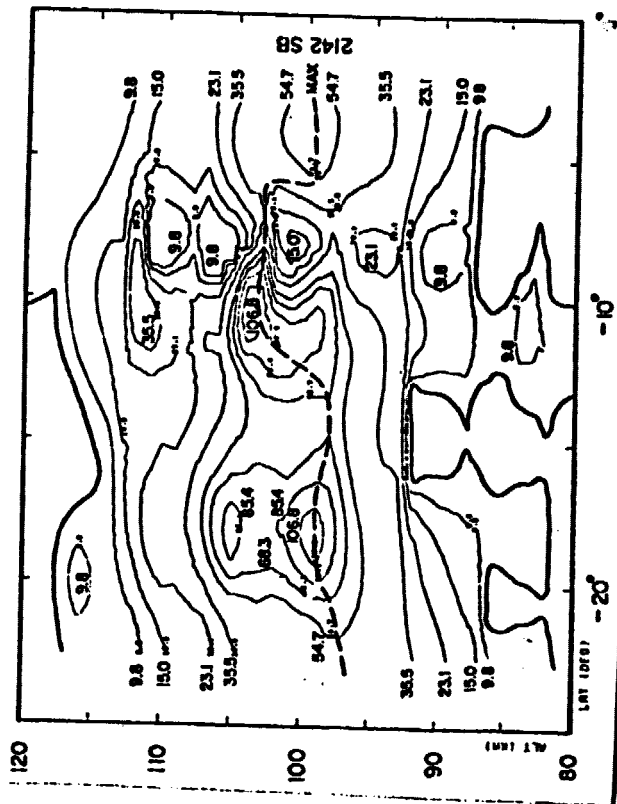
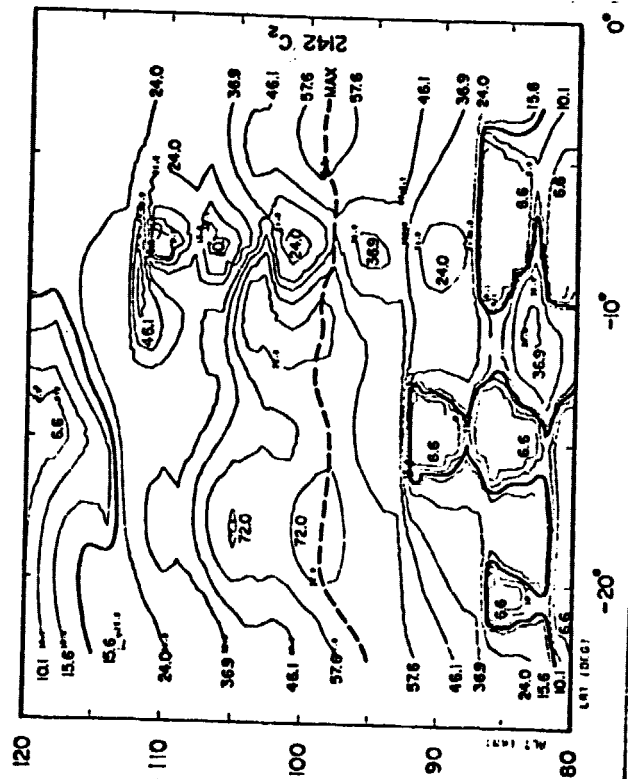
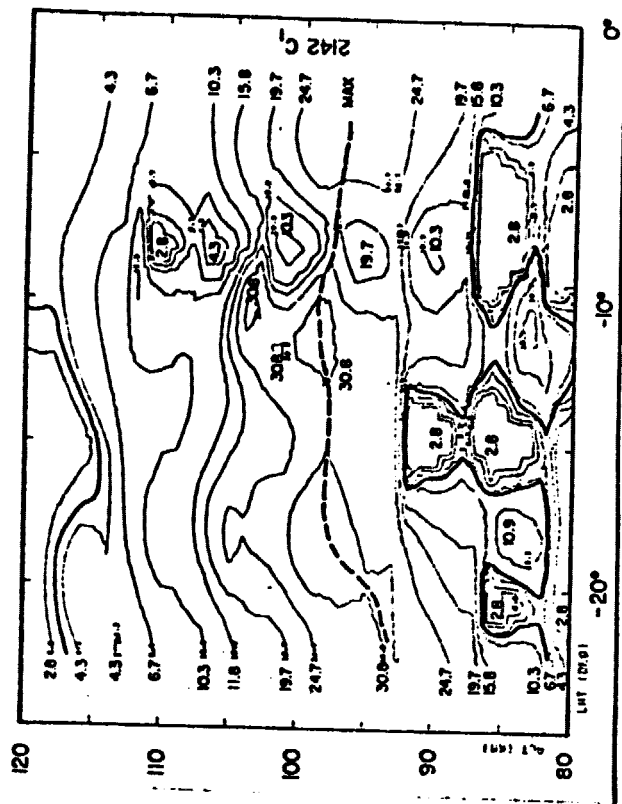
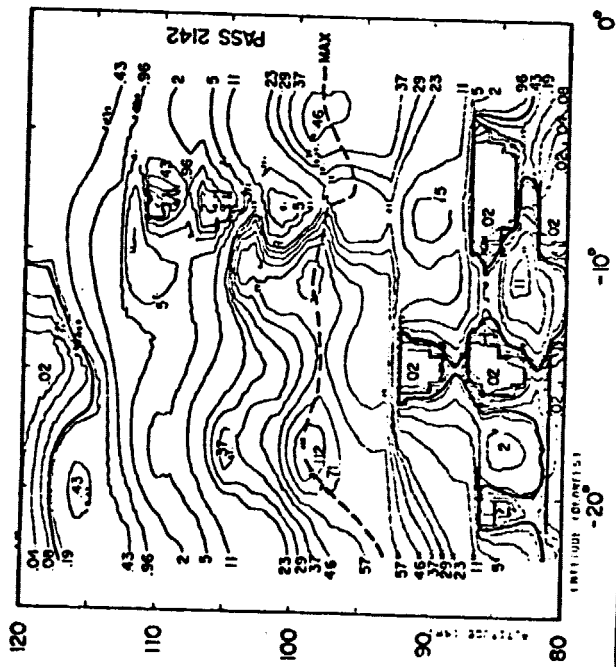


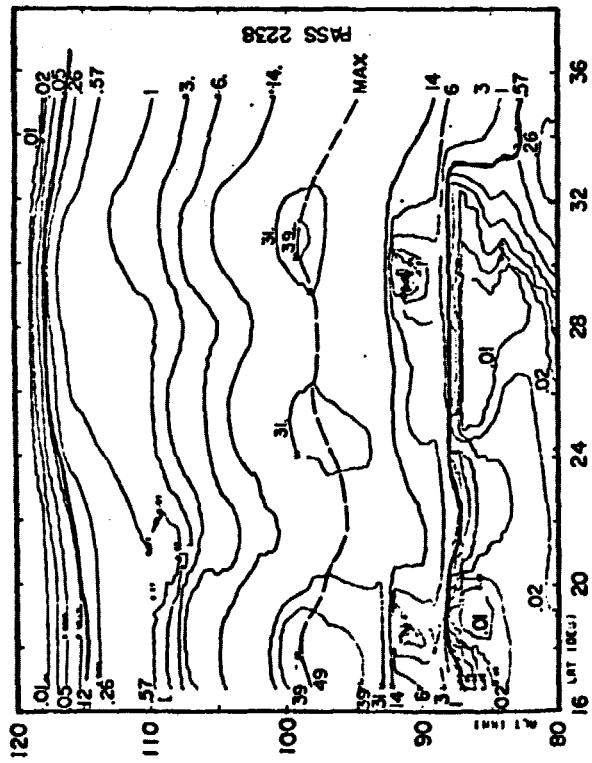
2a



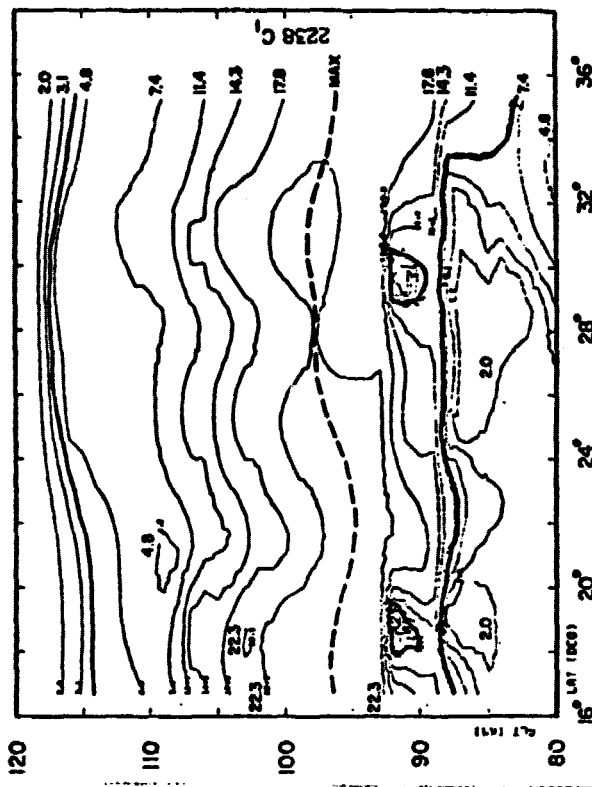
2b



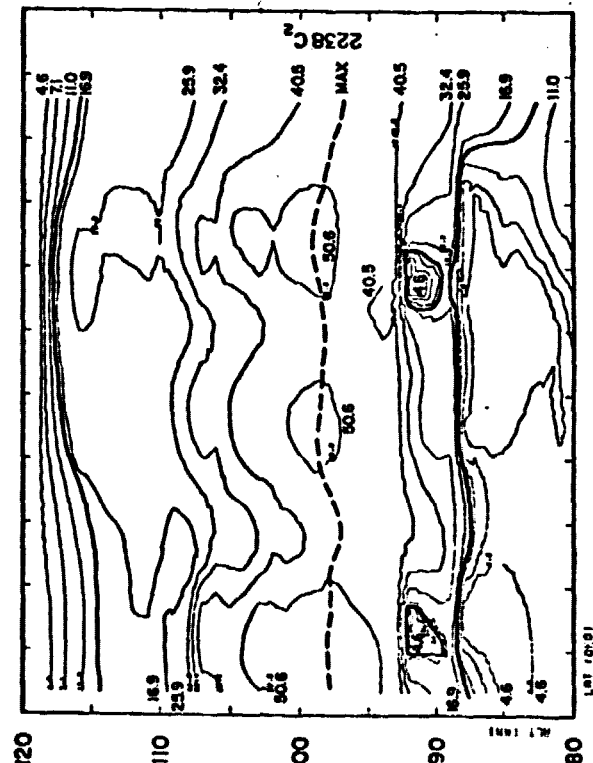




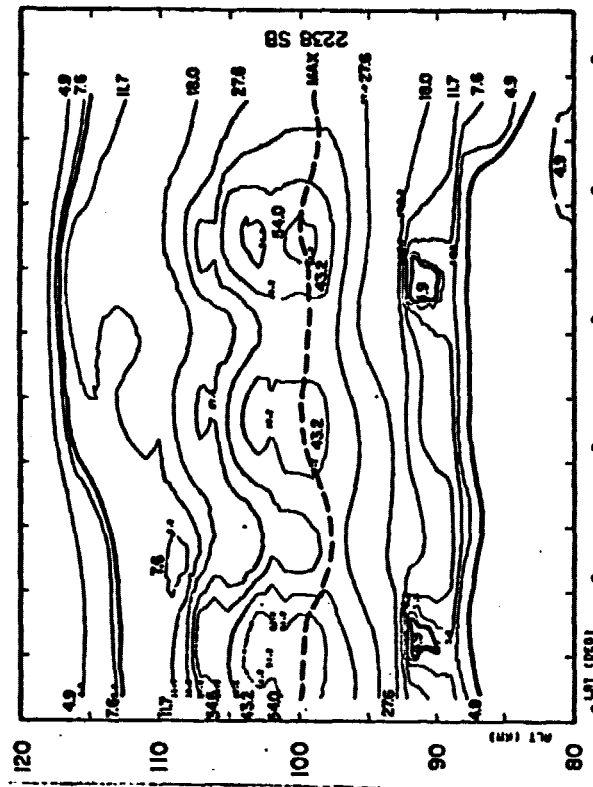
4a



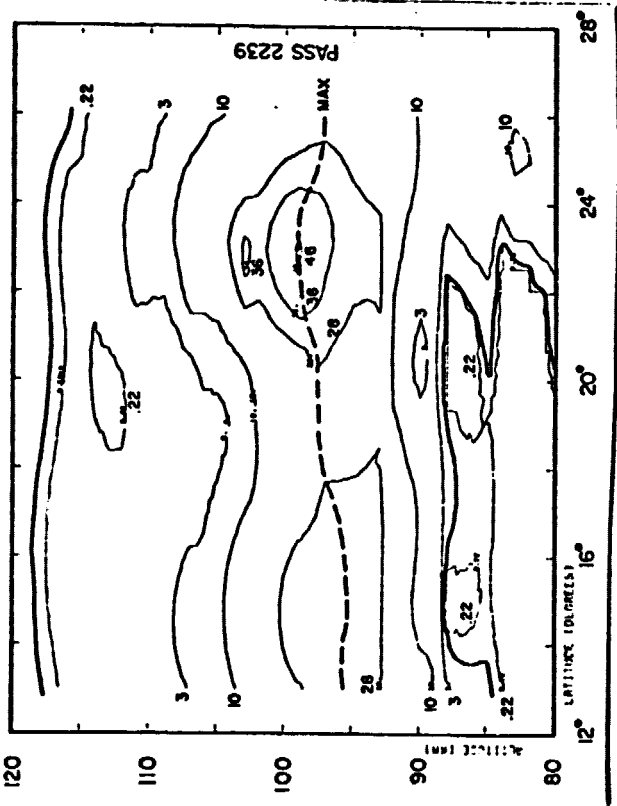
4b



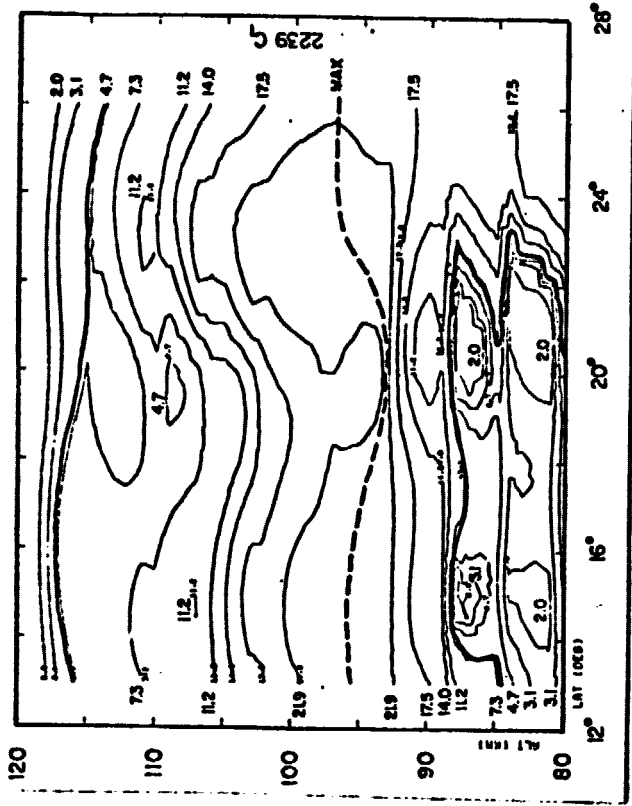
4c



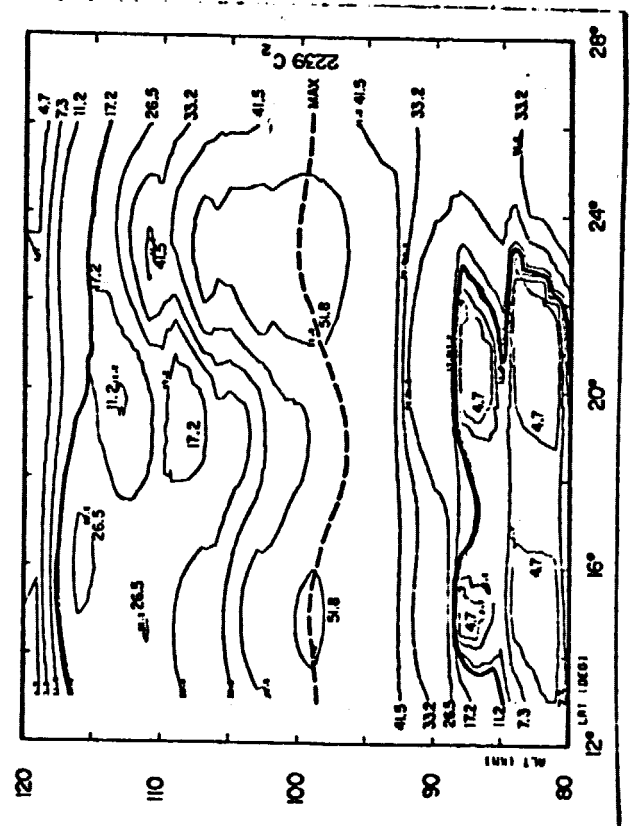
4d



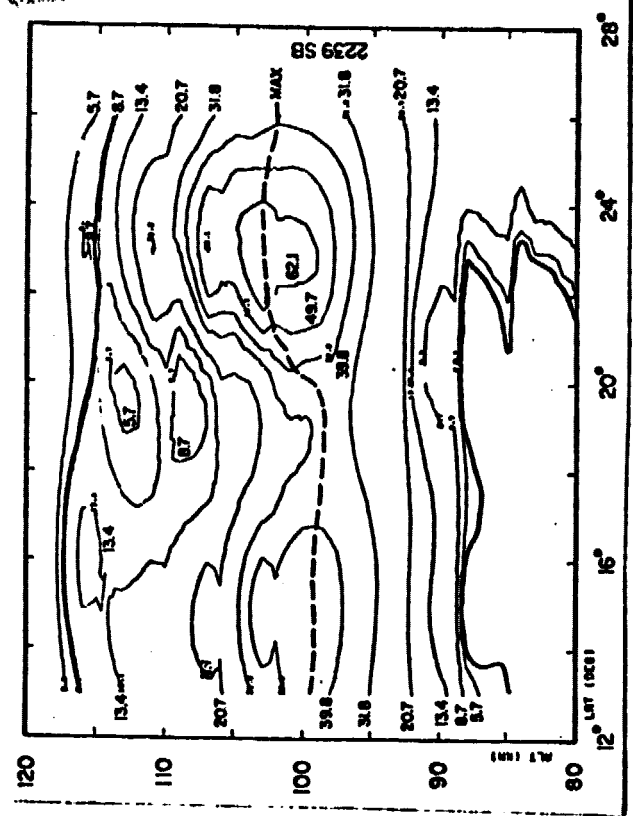
5a



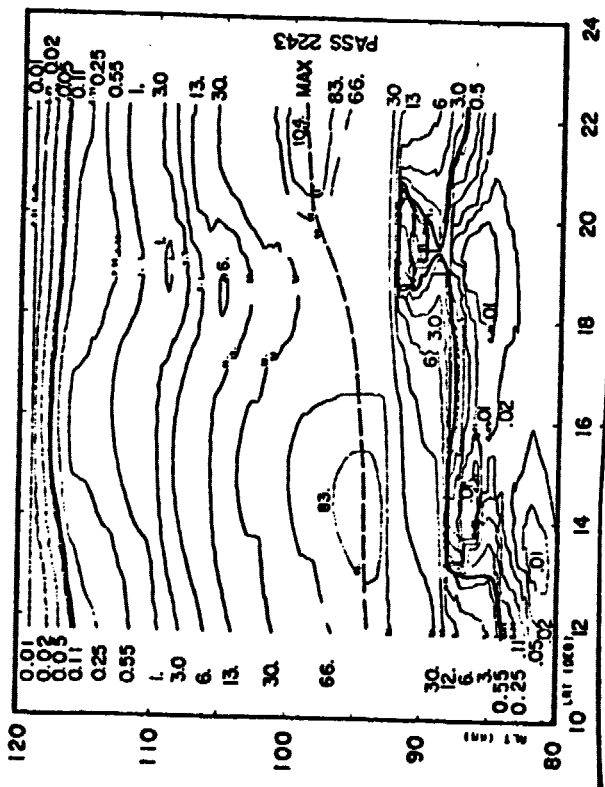
5b



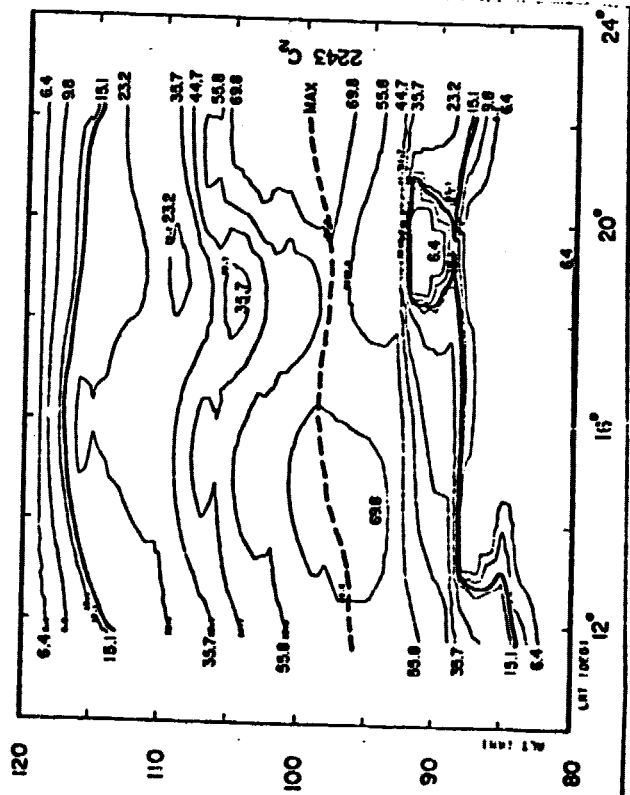
5c



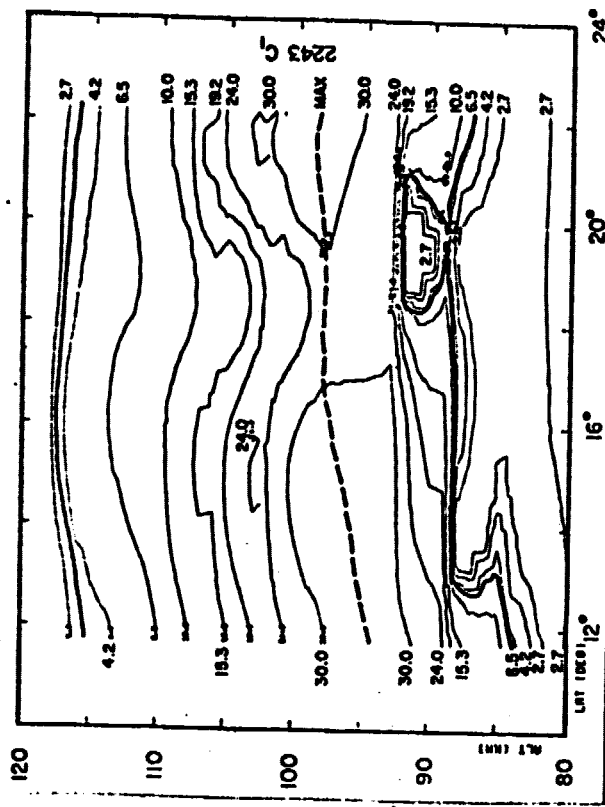
5d



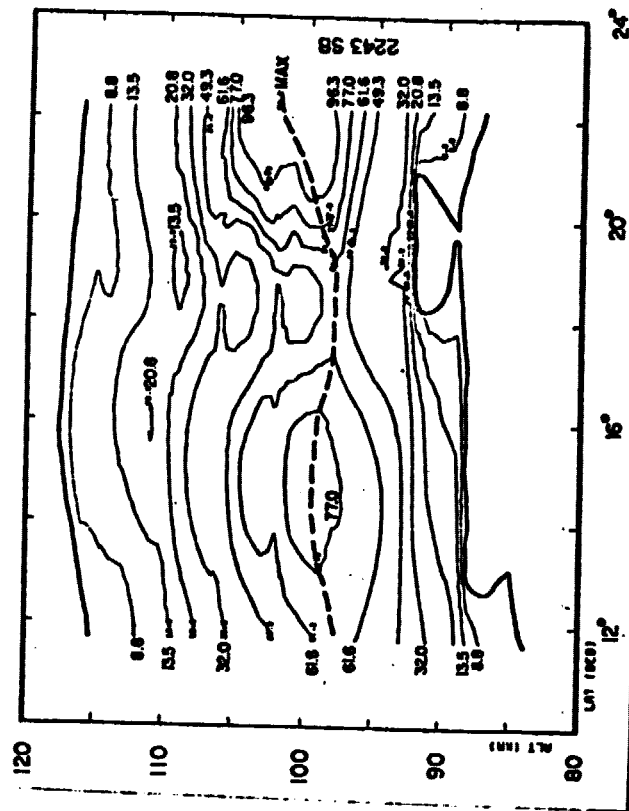
6a



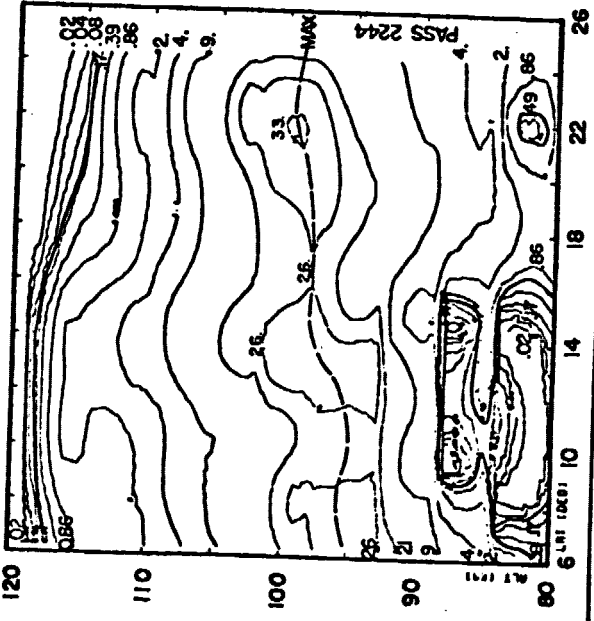
6c



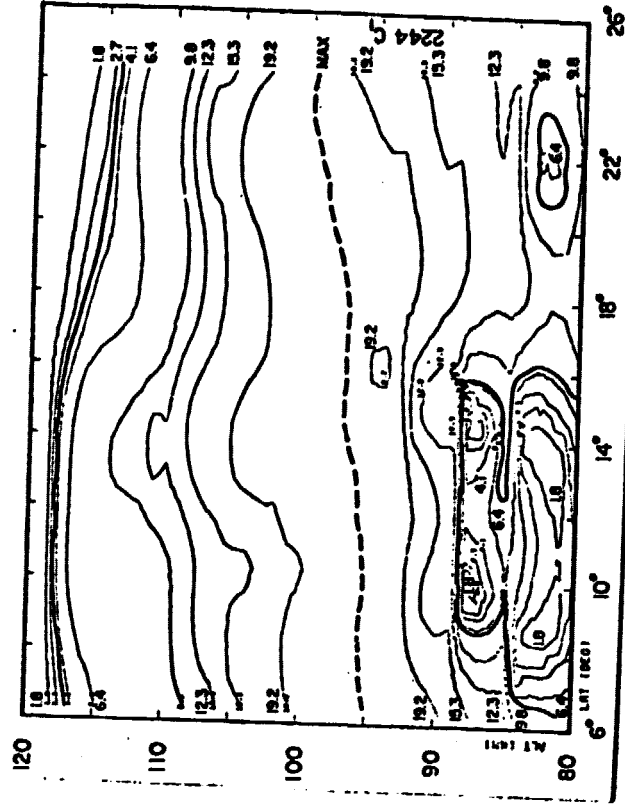
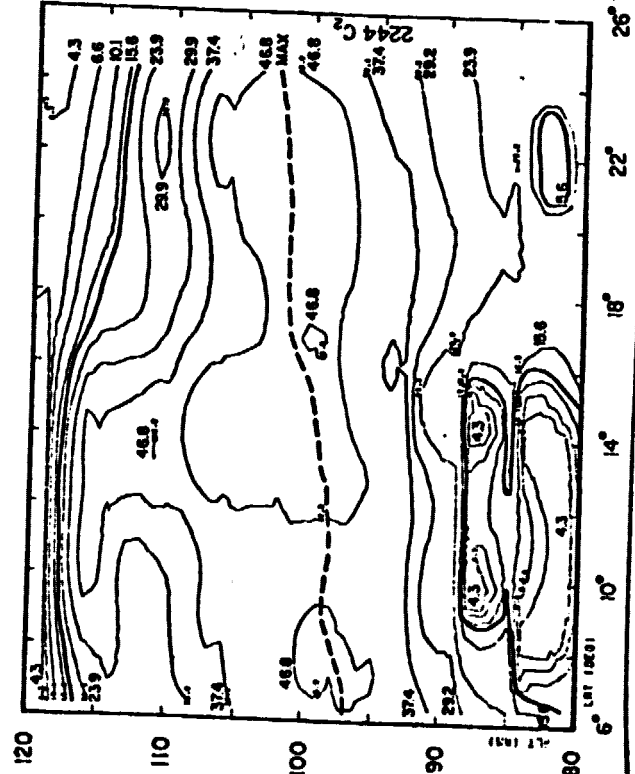
6b



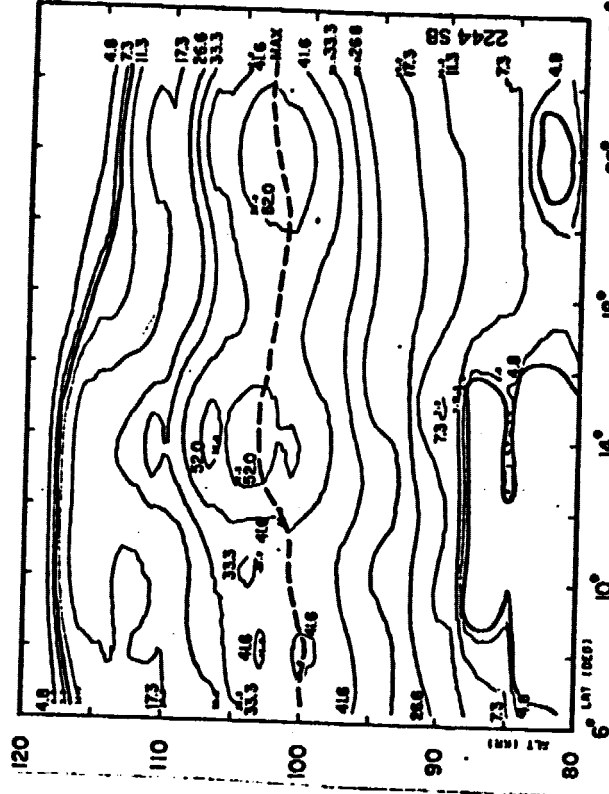
6d

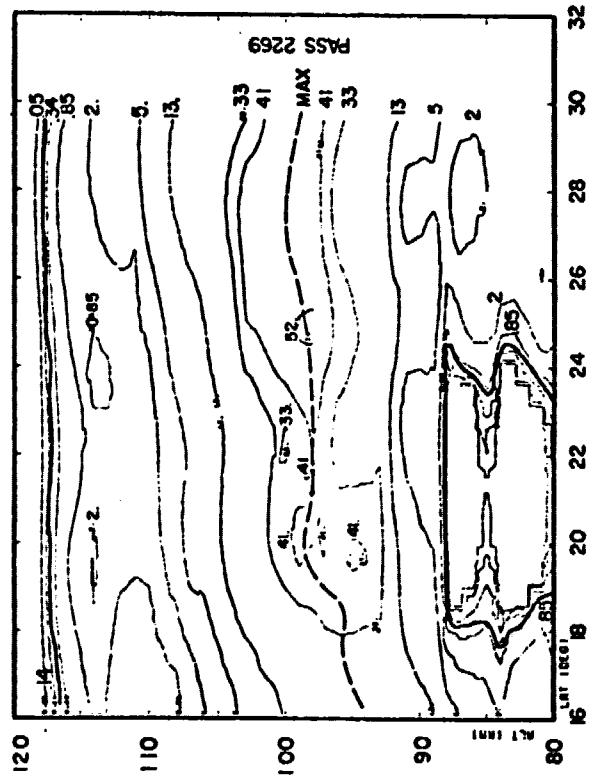


7a

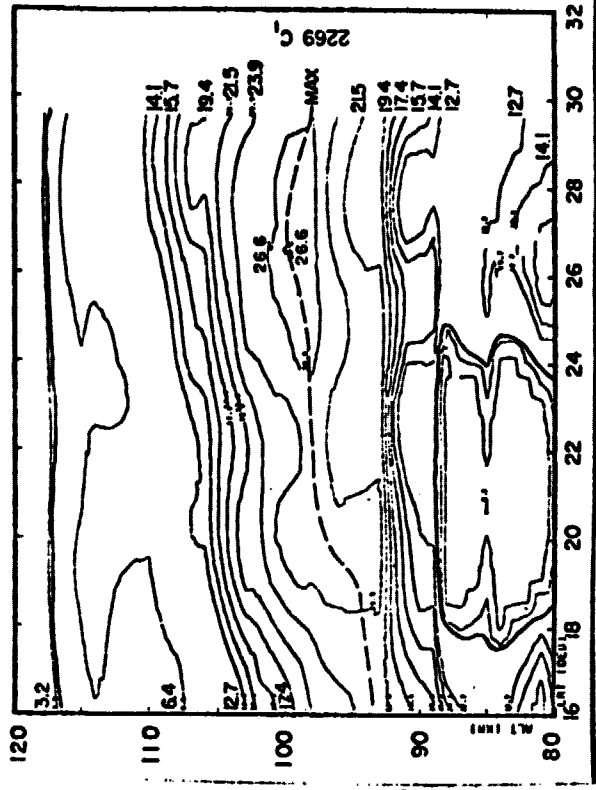


7b

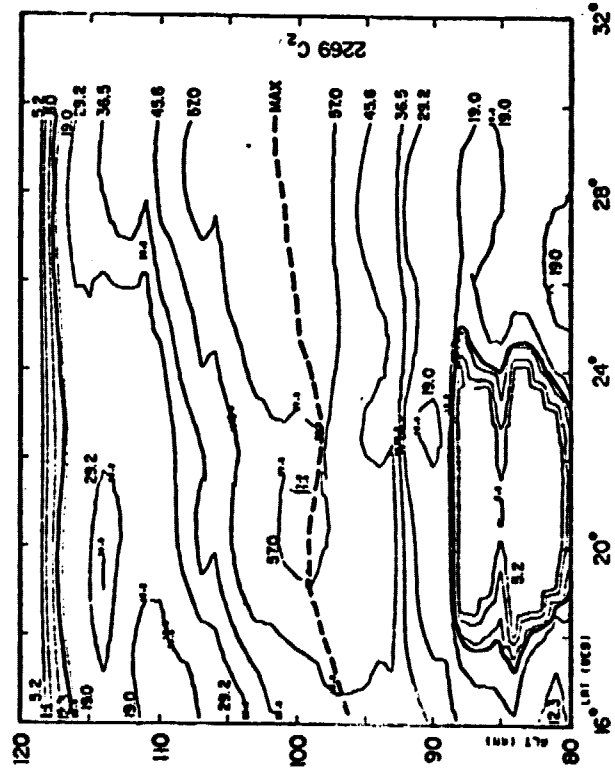




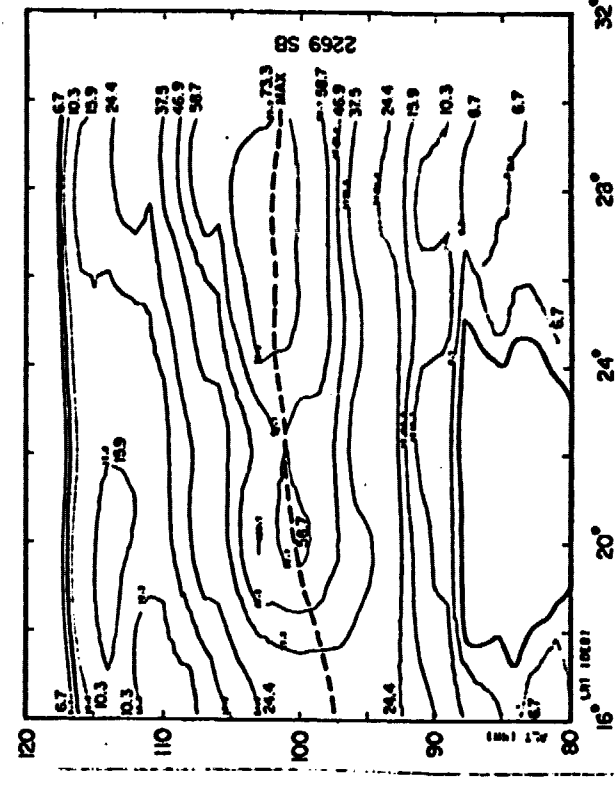
8a



8b



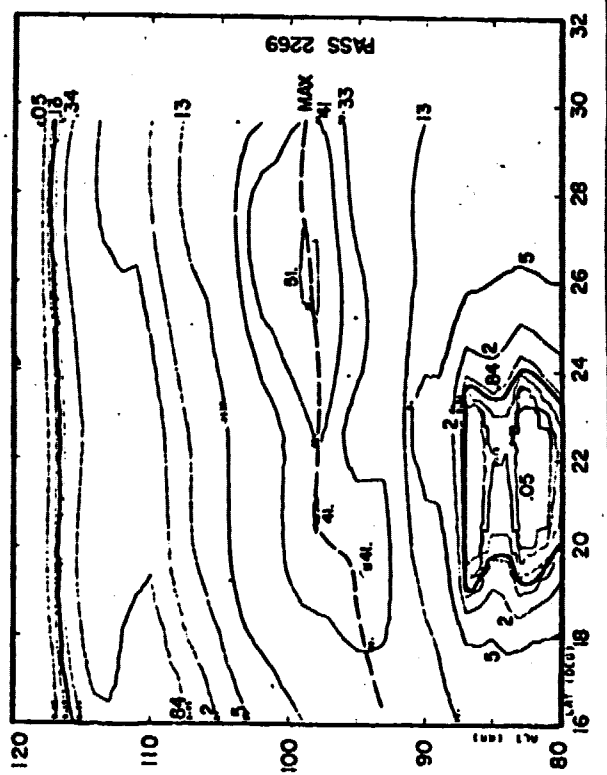
8c

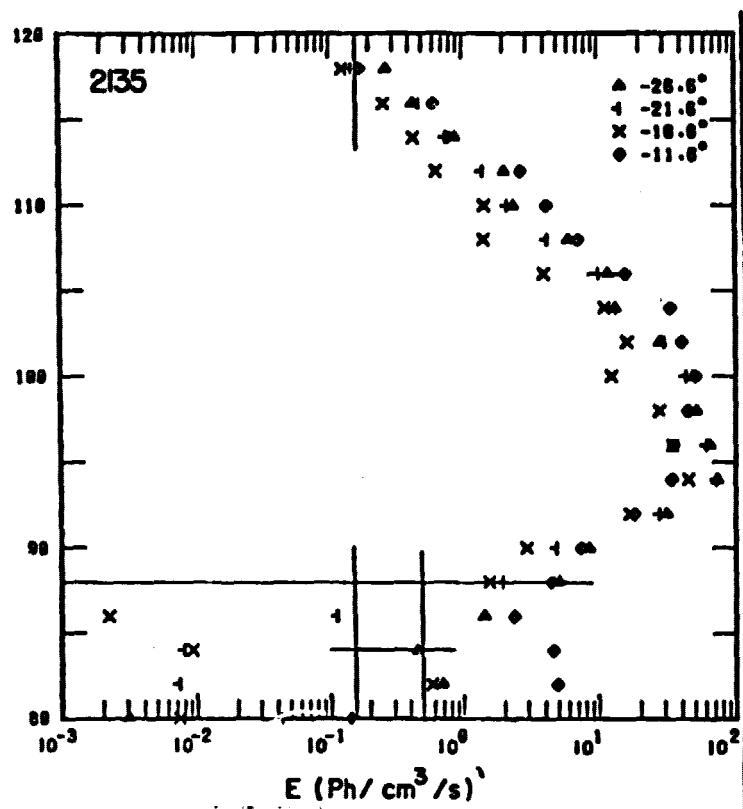


8d

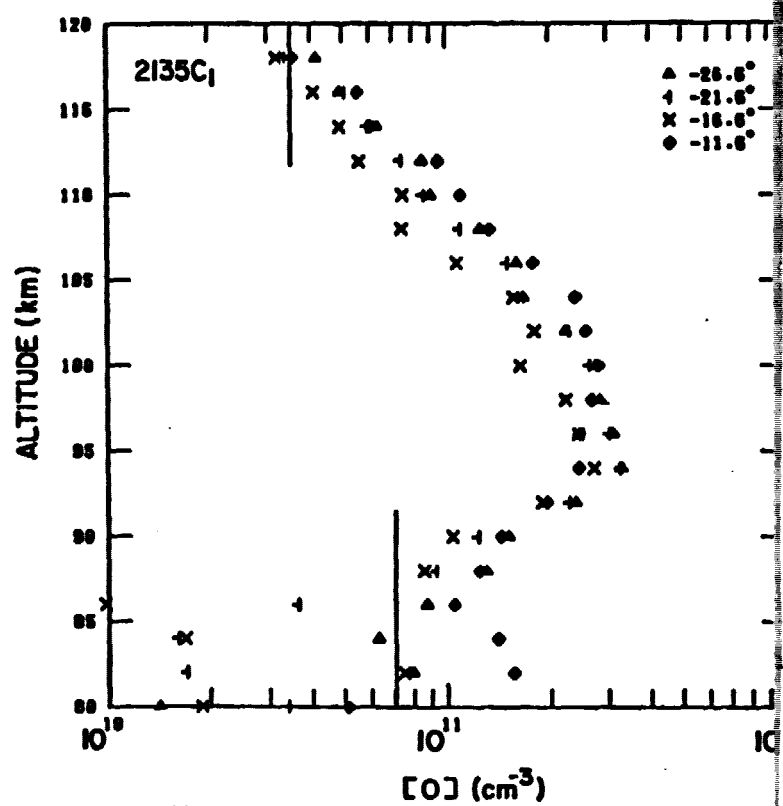
50



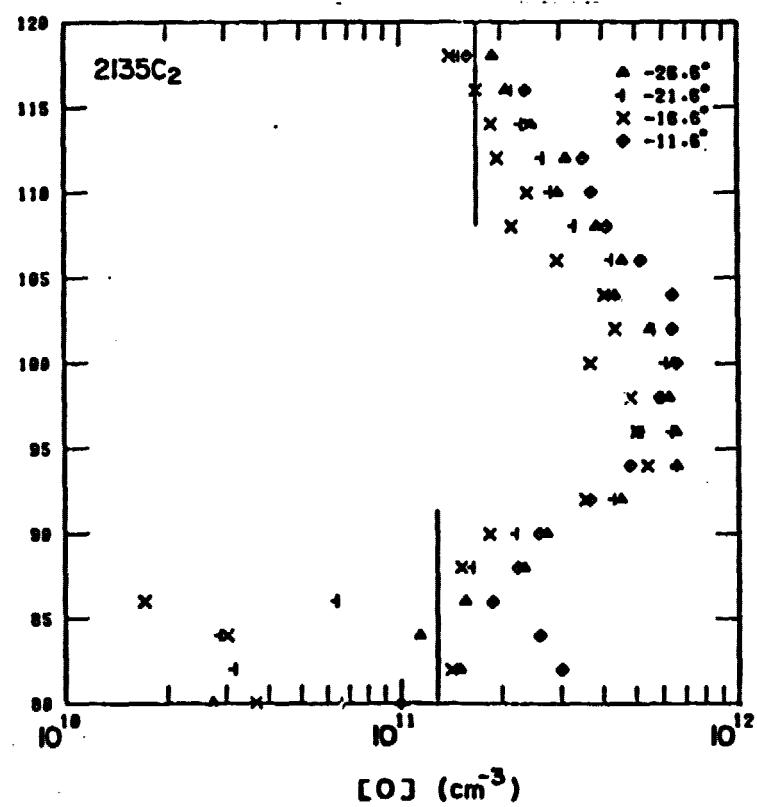




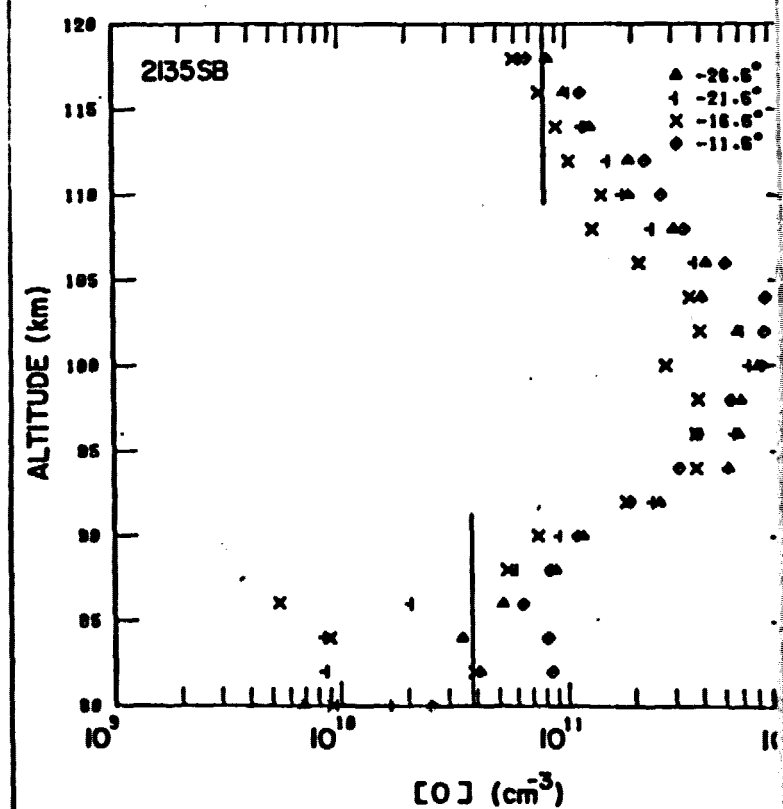
11a



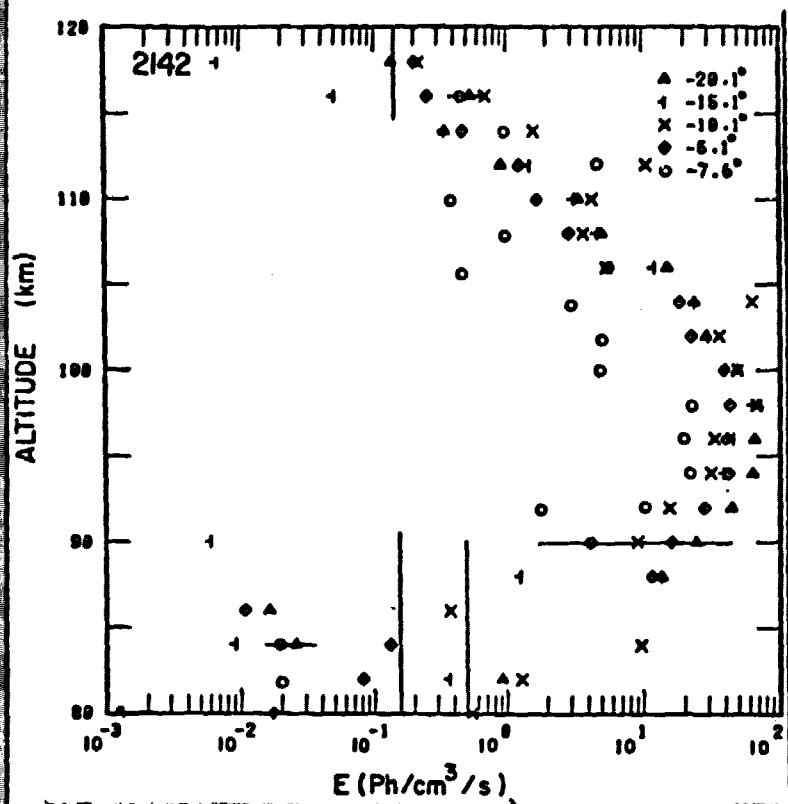
11b



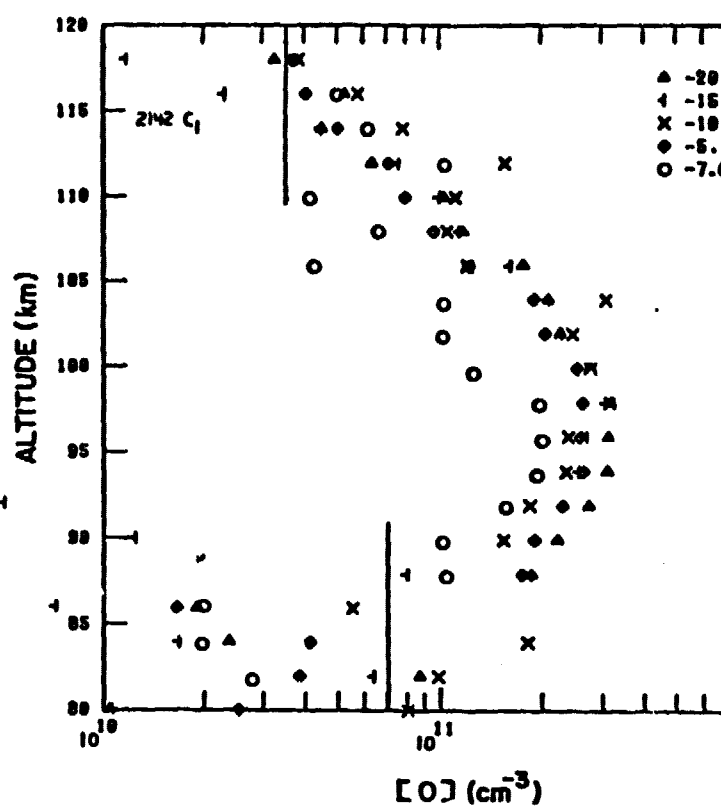
11c



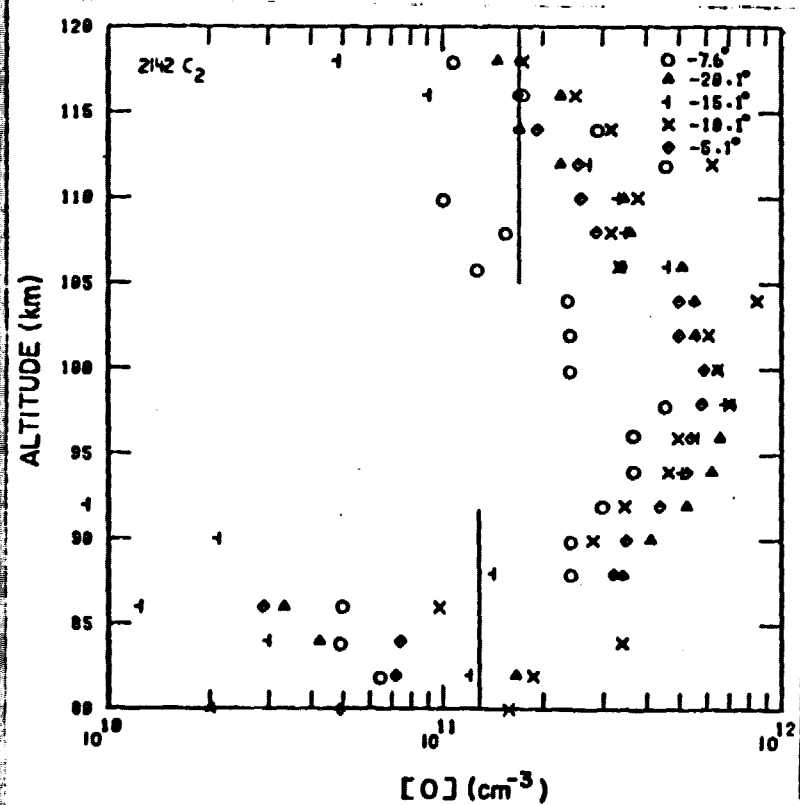
11d



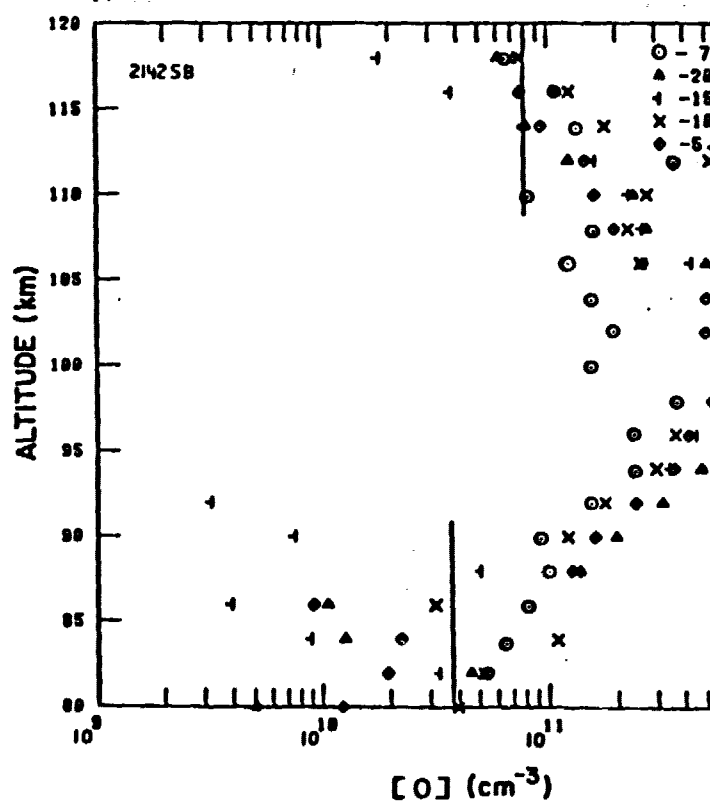
12 a

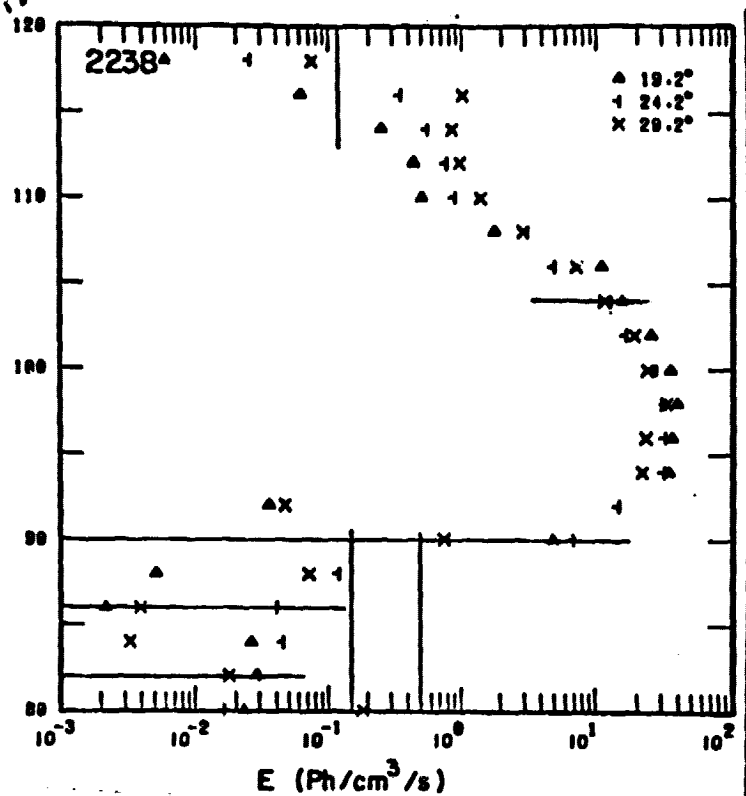


12 b

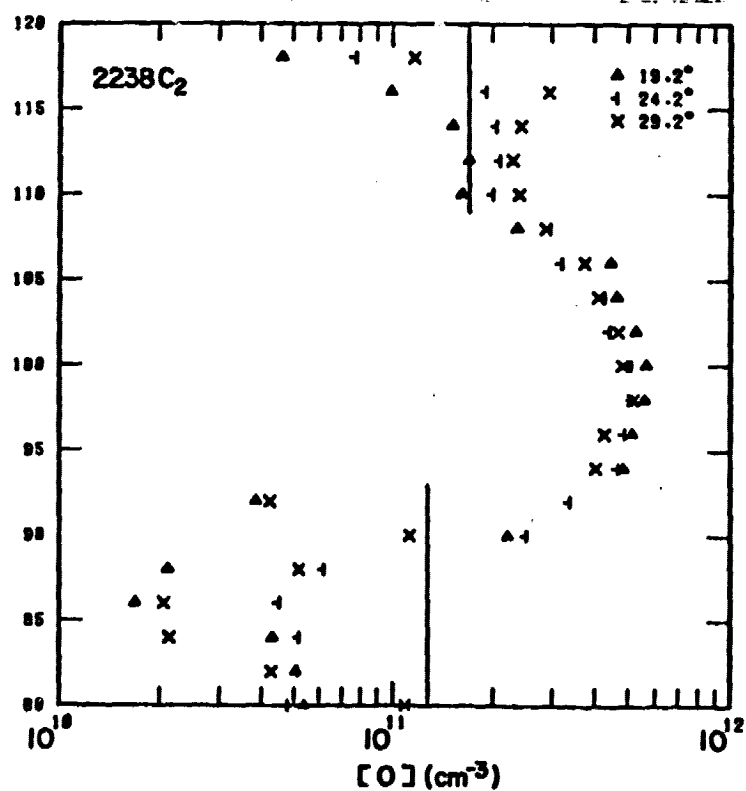
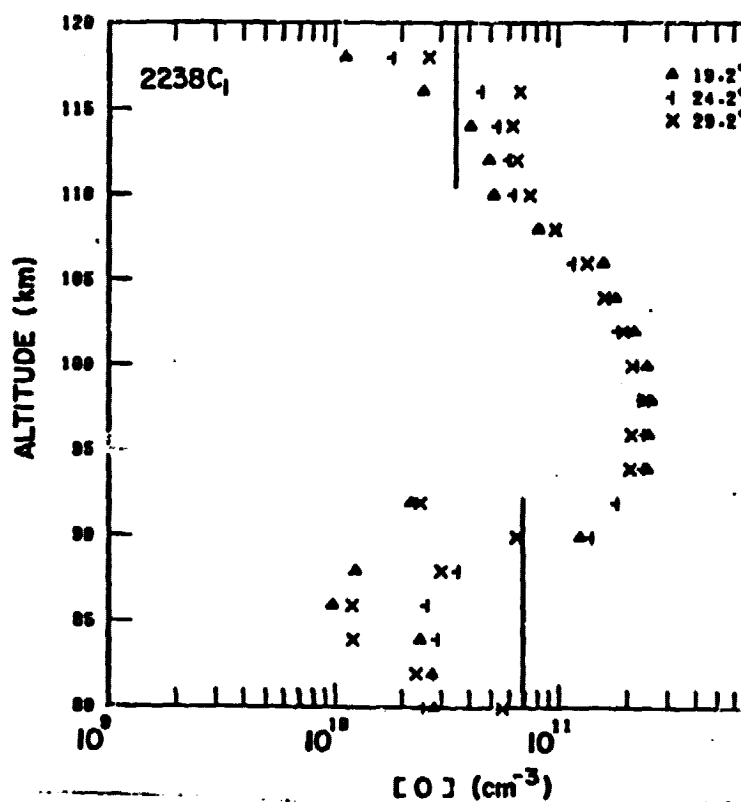


12 c

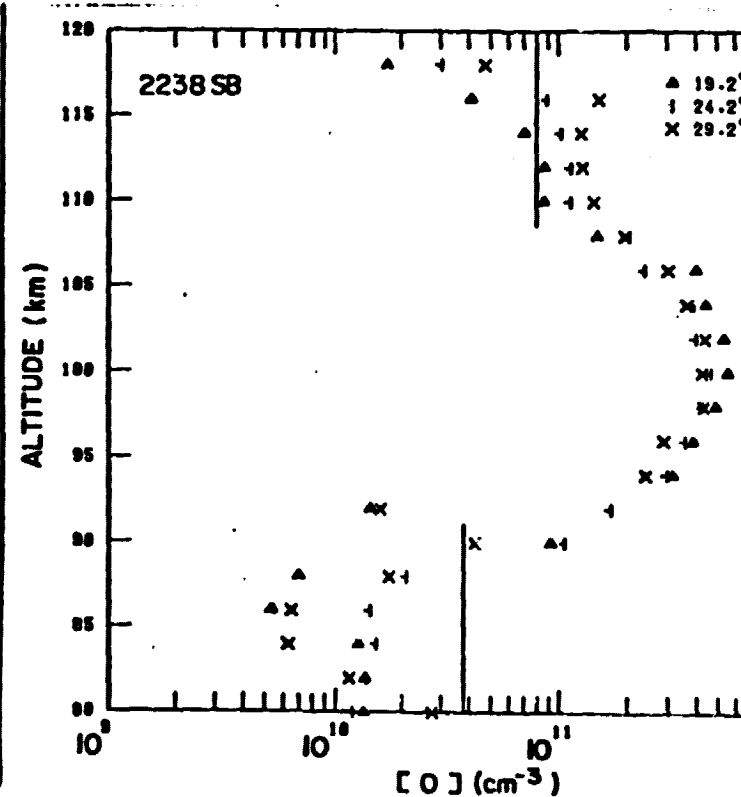




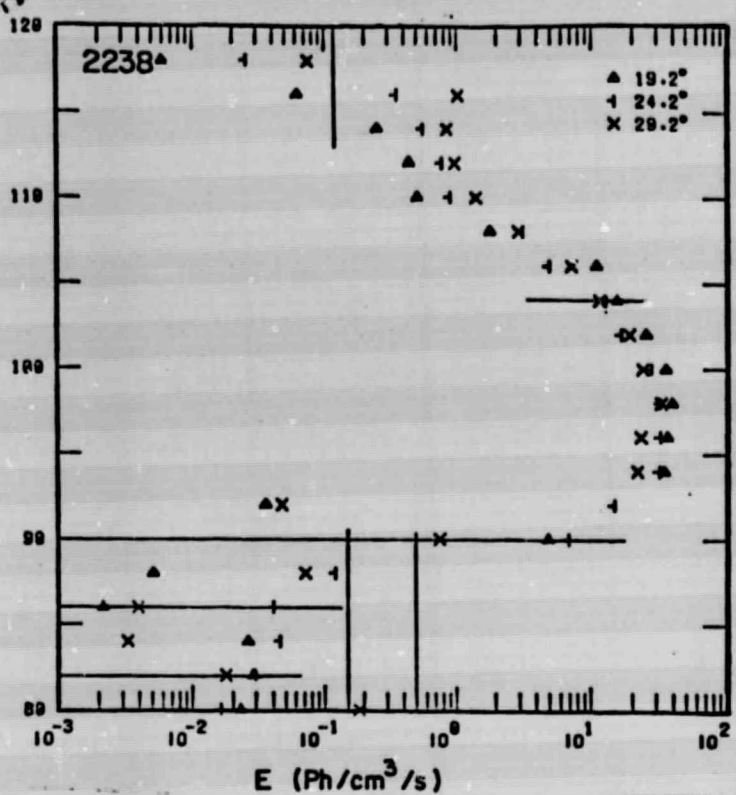
13a



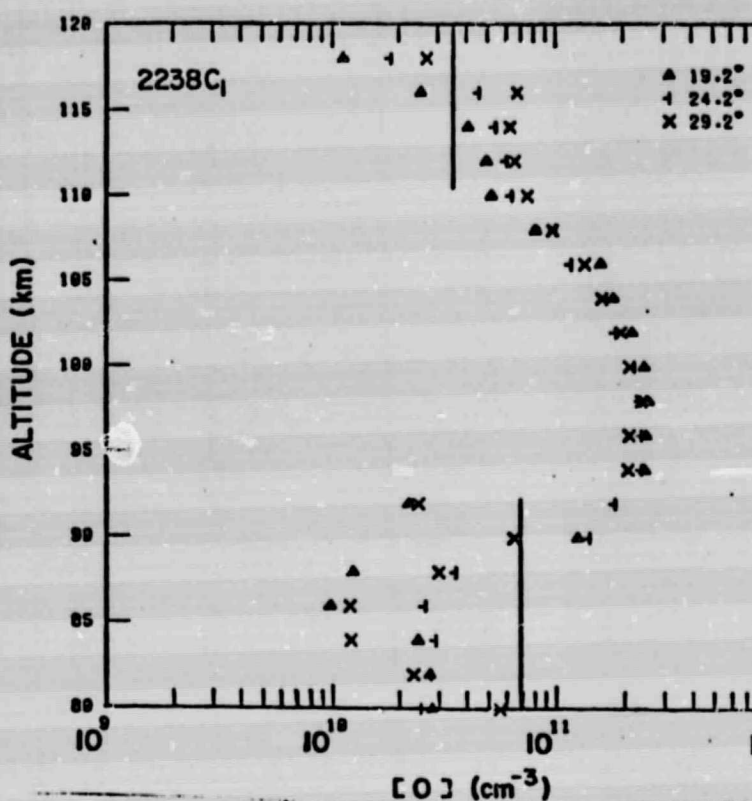
13c



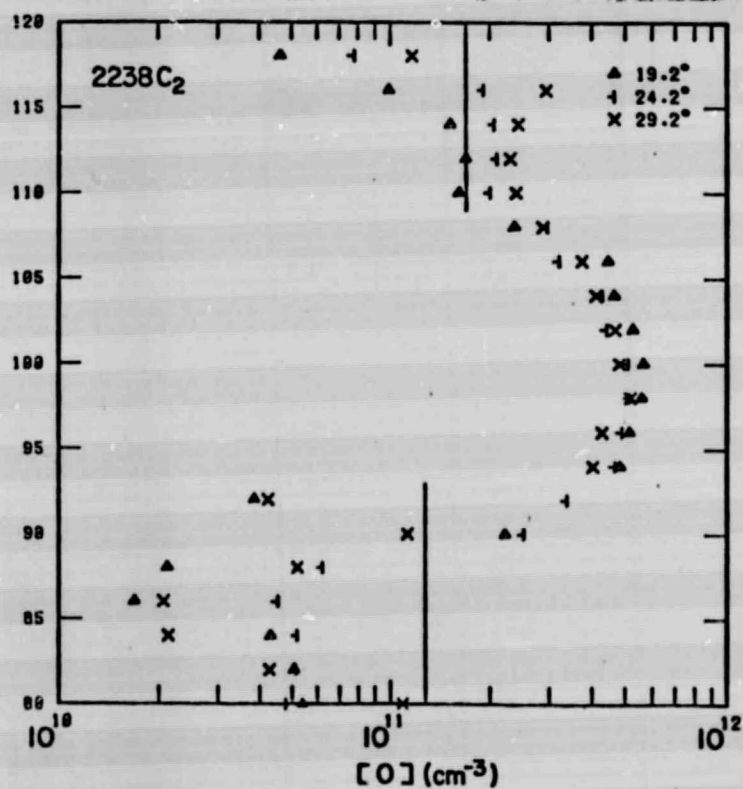
13



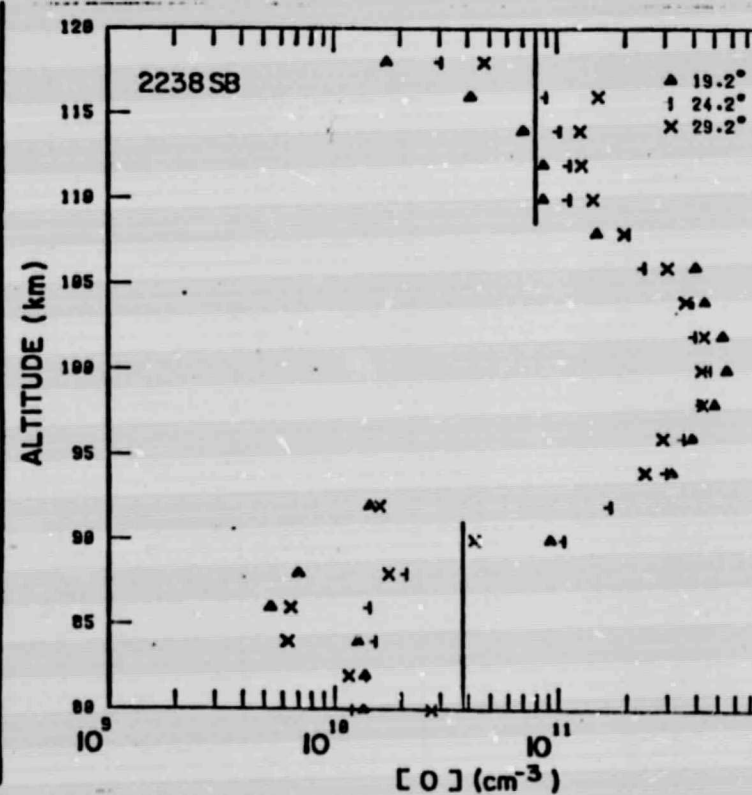
13a



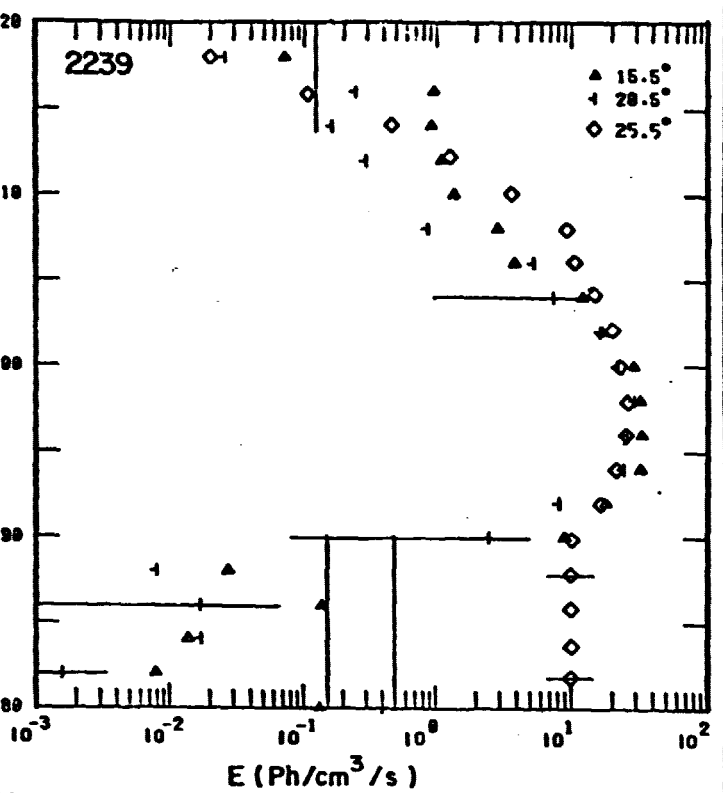
13



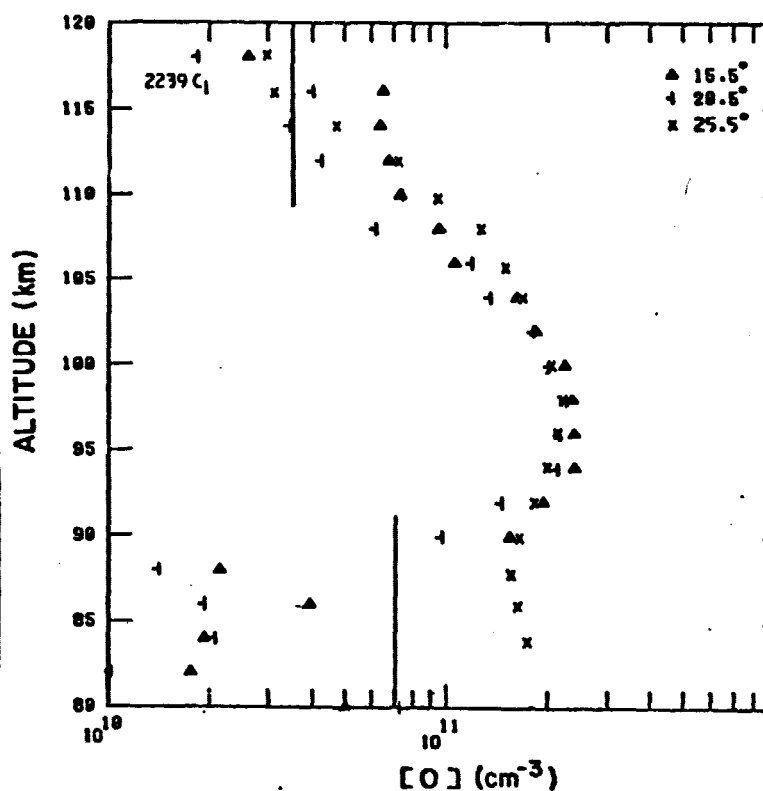
13c



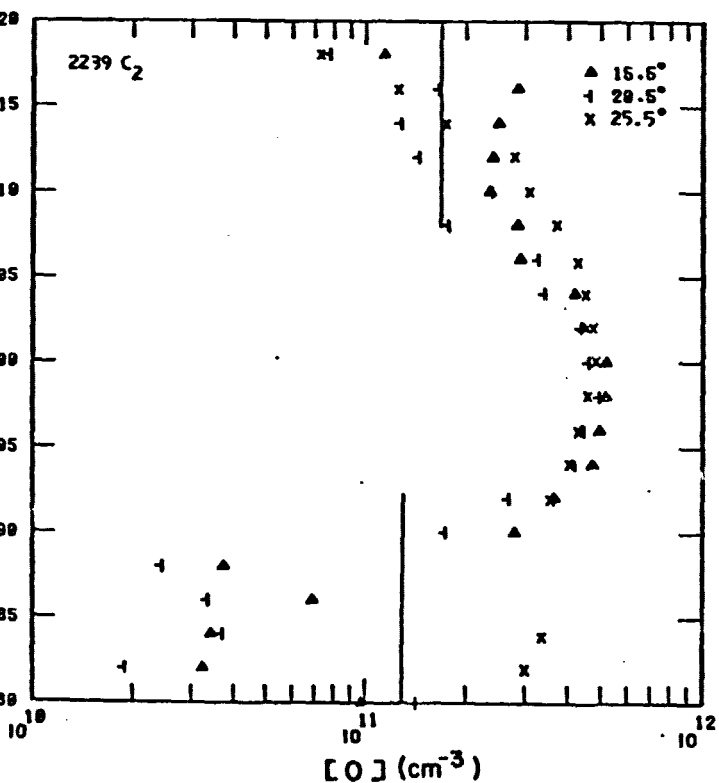
13



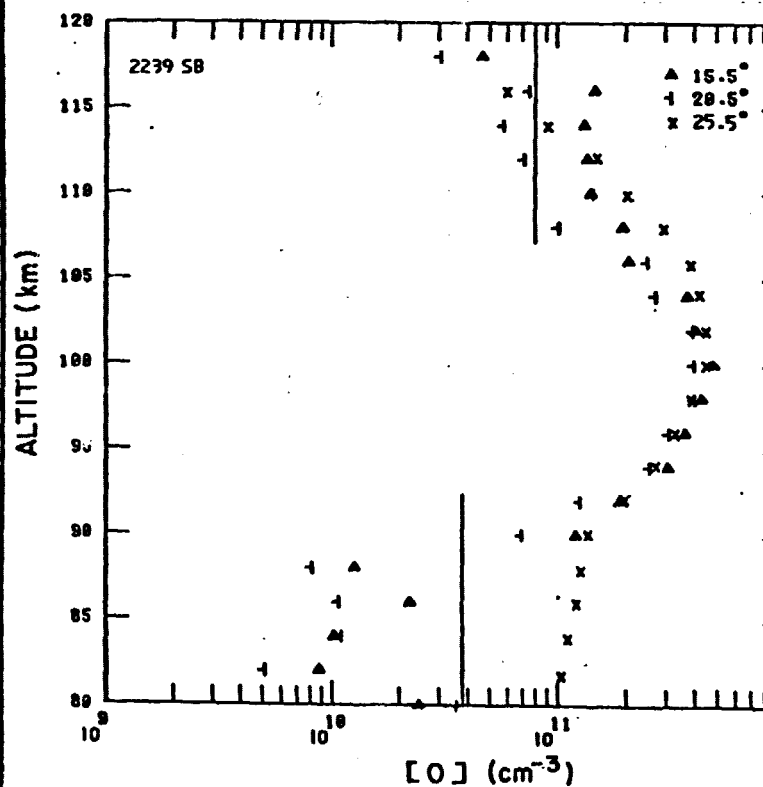
14a



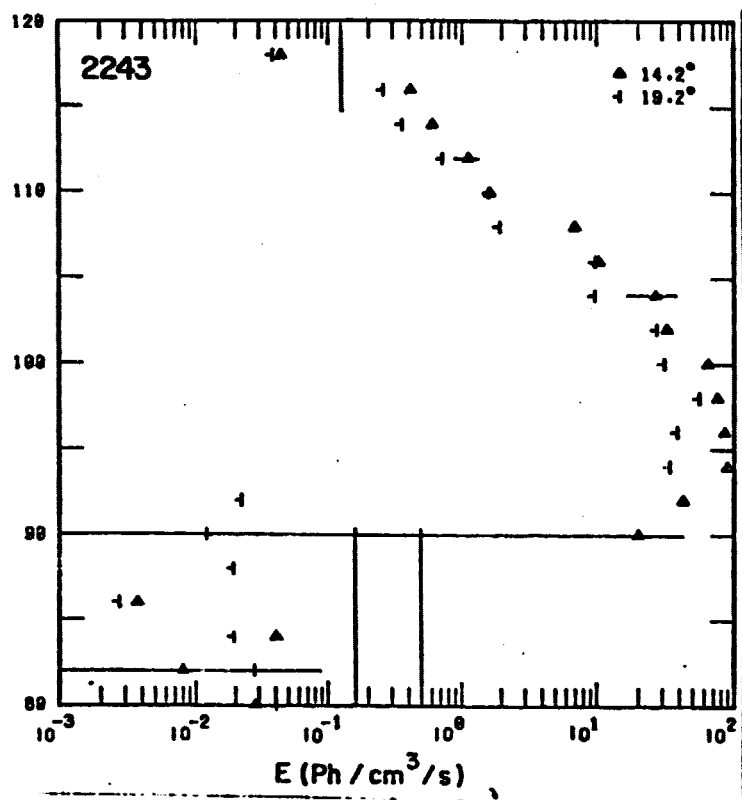
14b



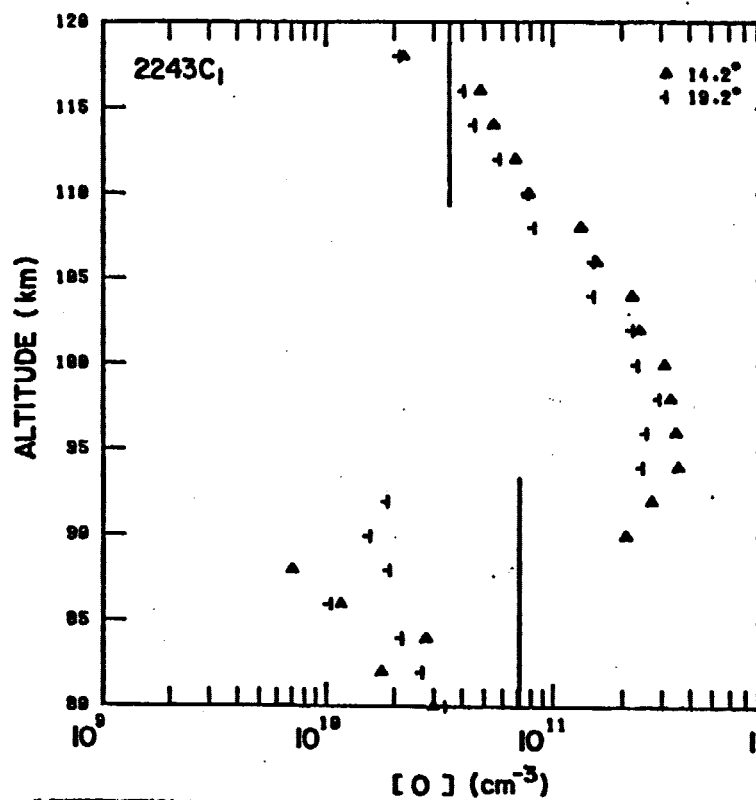
14c



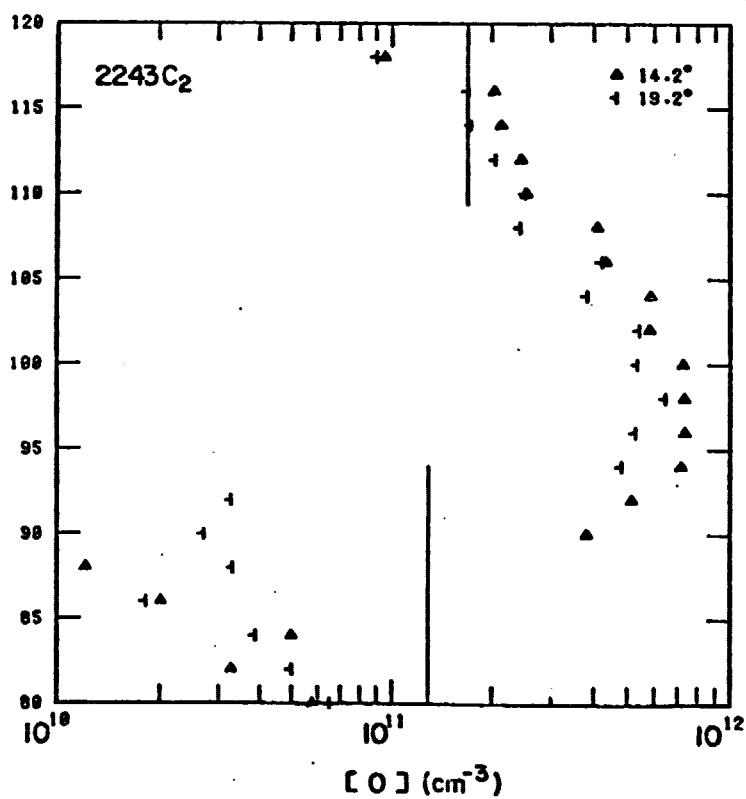
14d



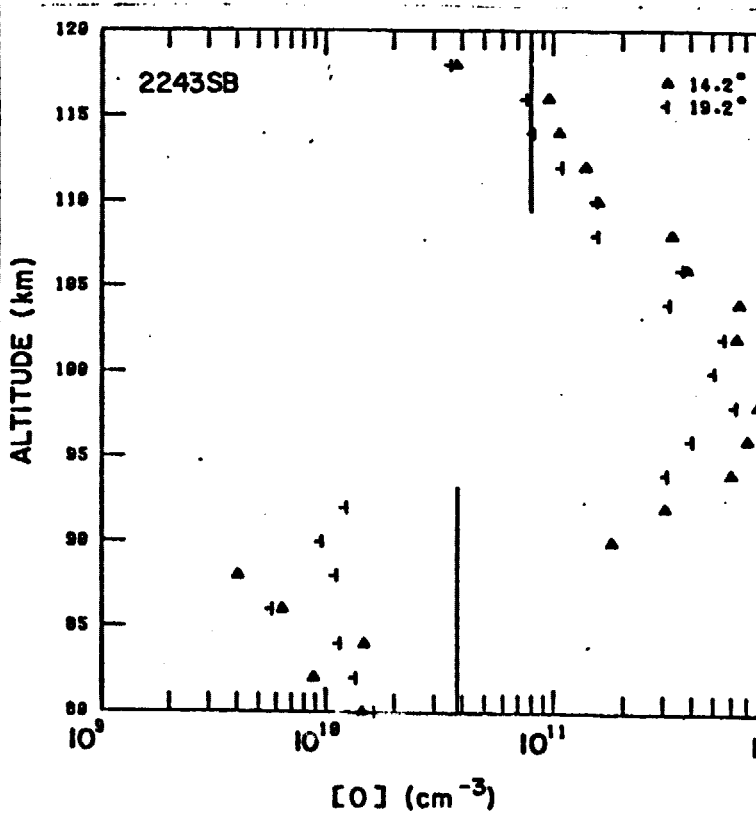
15a



15b

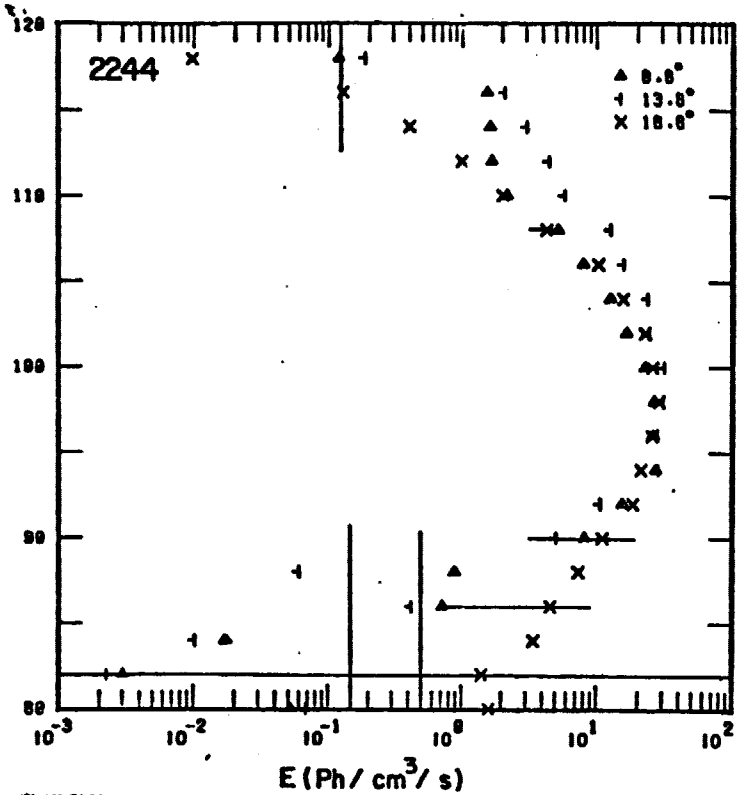


15c

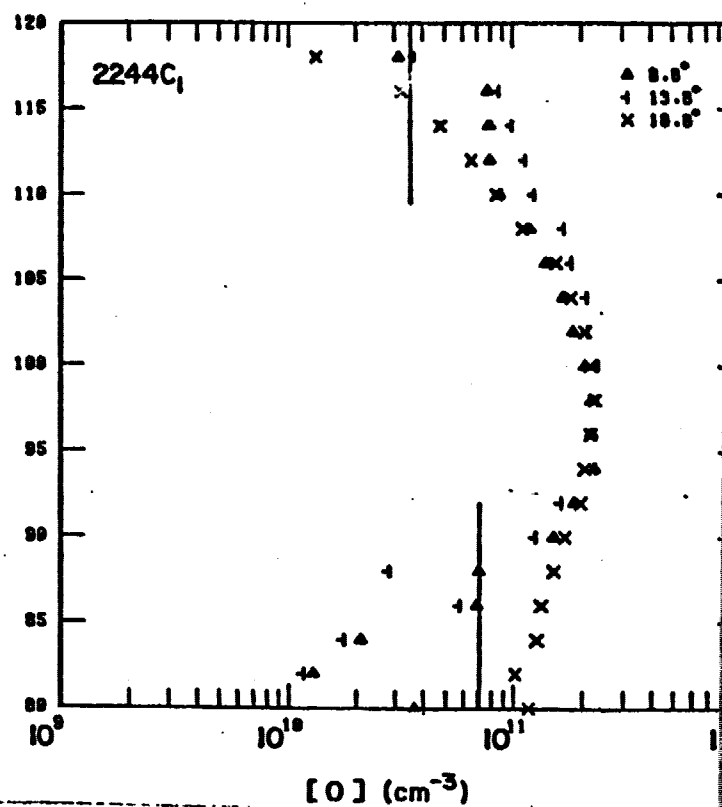


15d

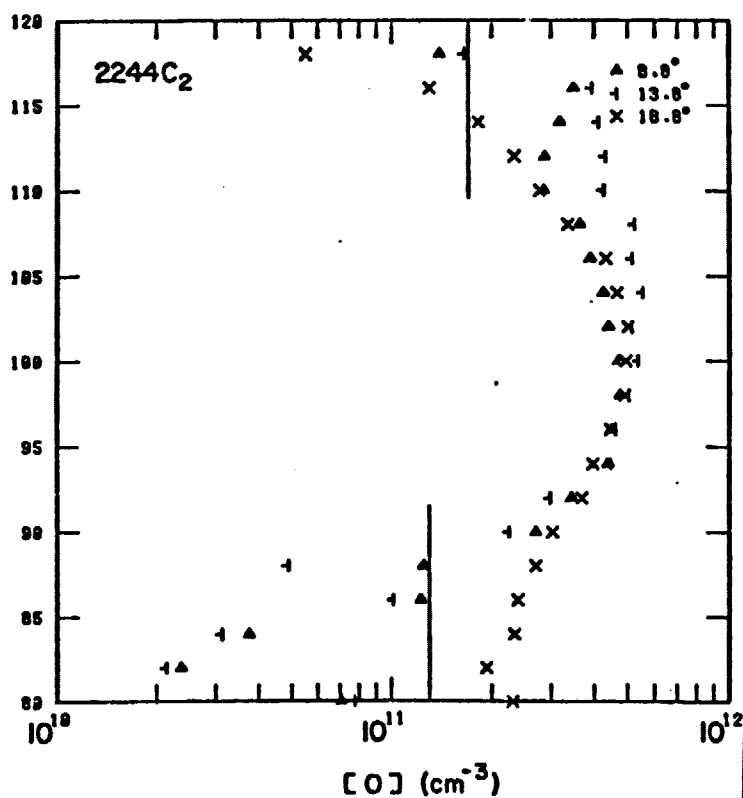
ALTITUDE (km)



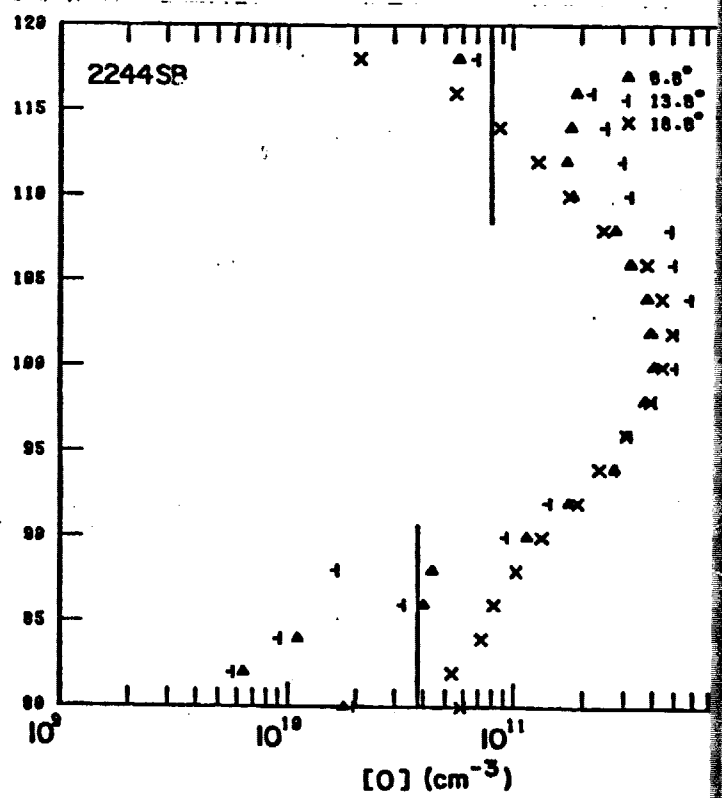
ALTITUDE (km)

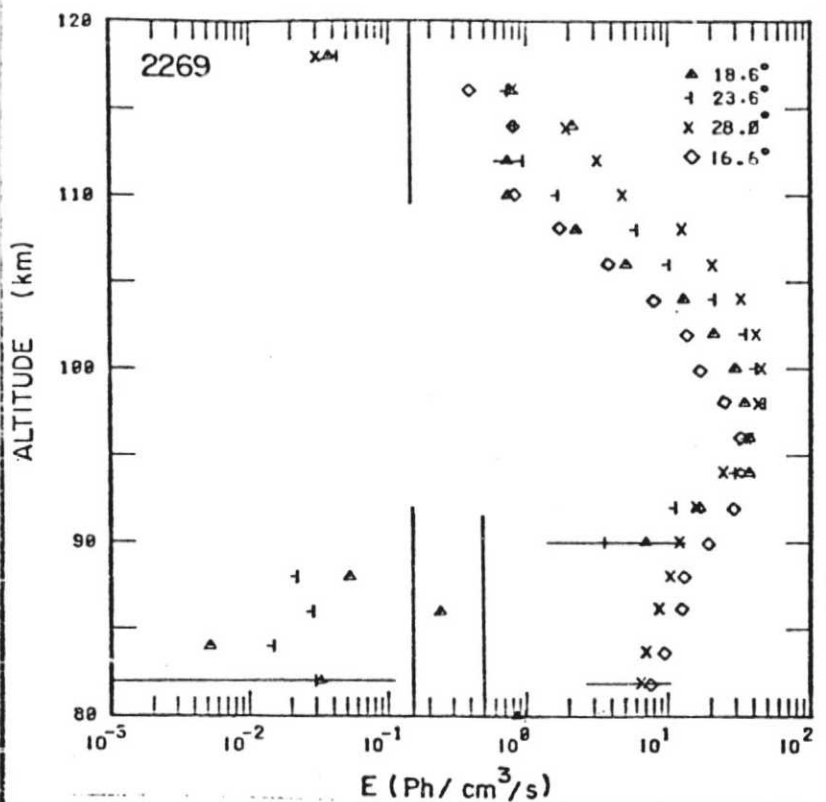


ALTITUDE (km)

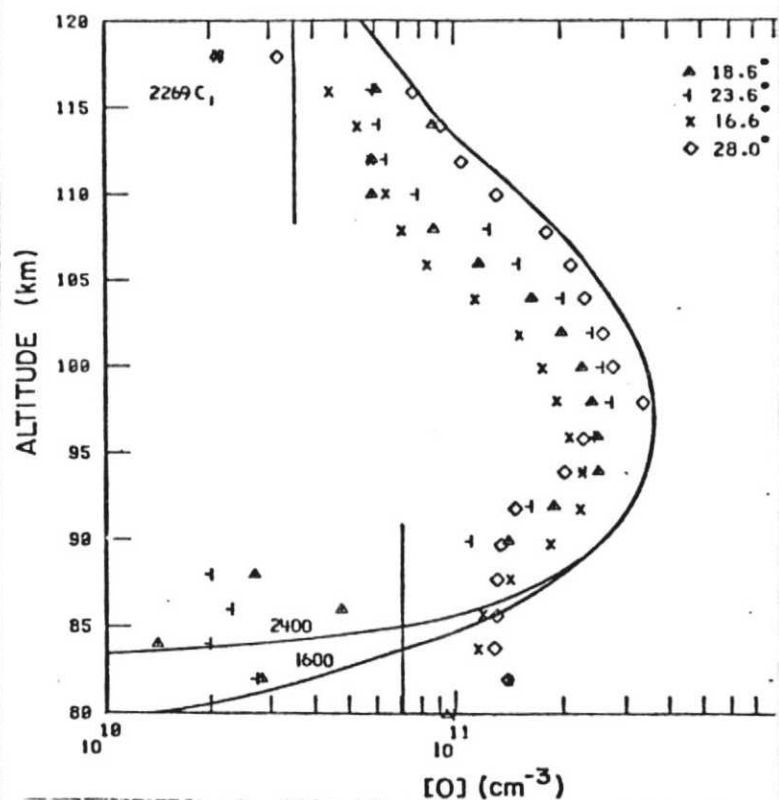


ALTITUDE (km)

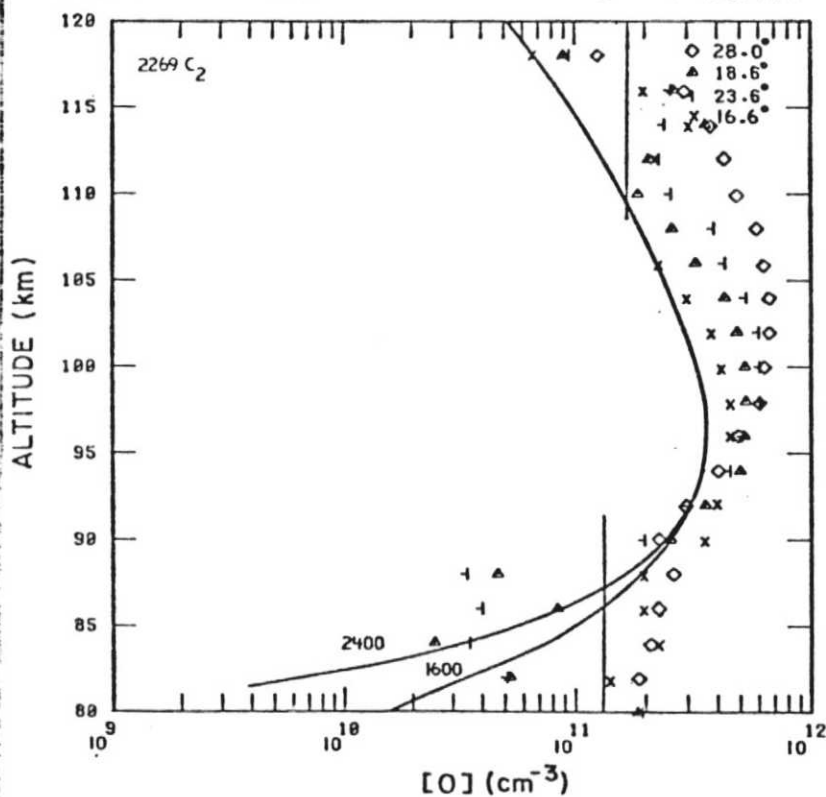




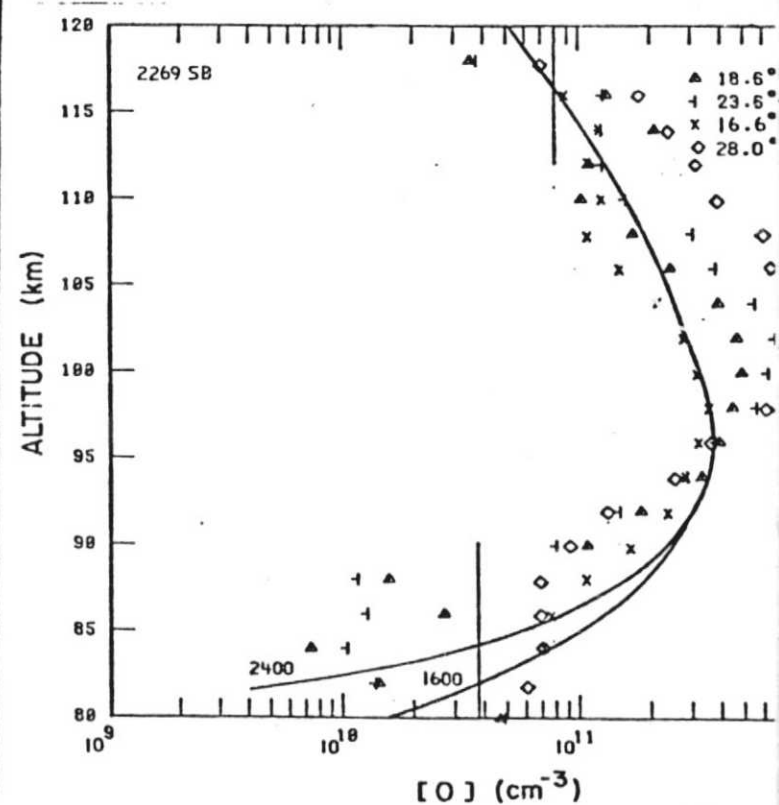
17a



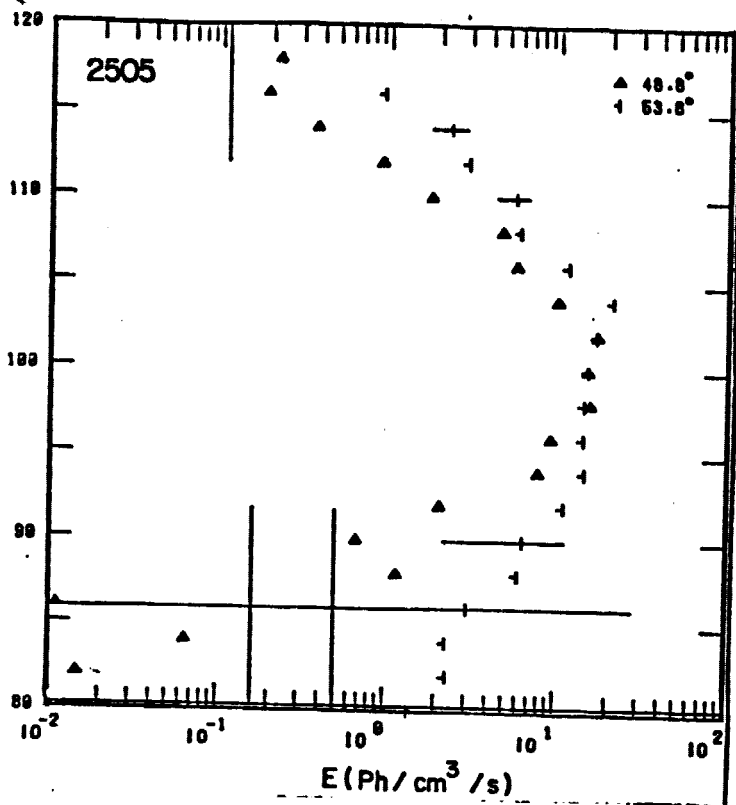
17



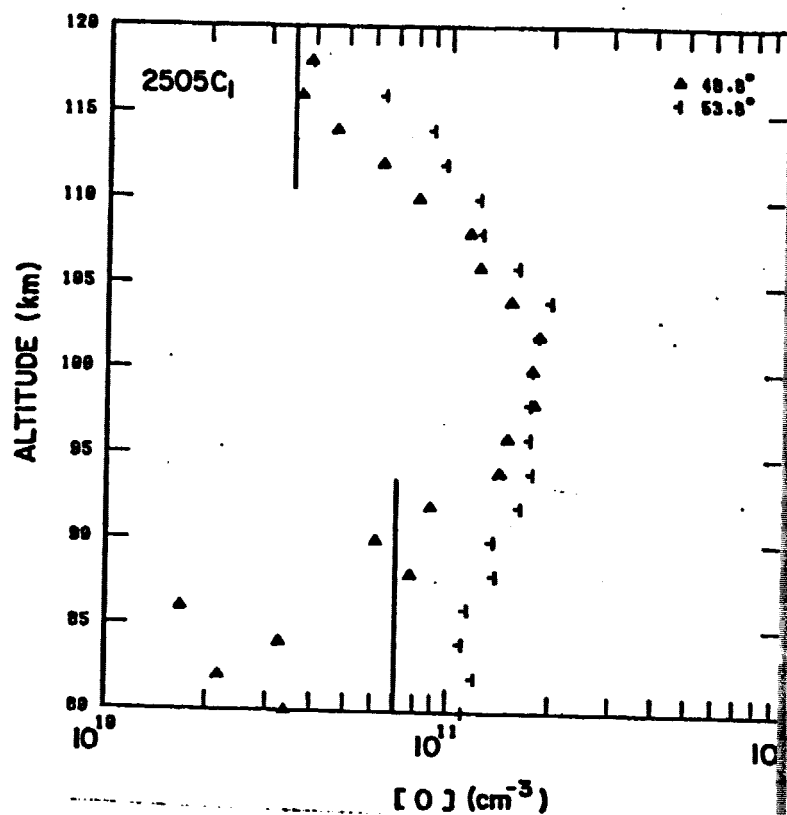
17c



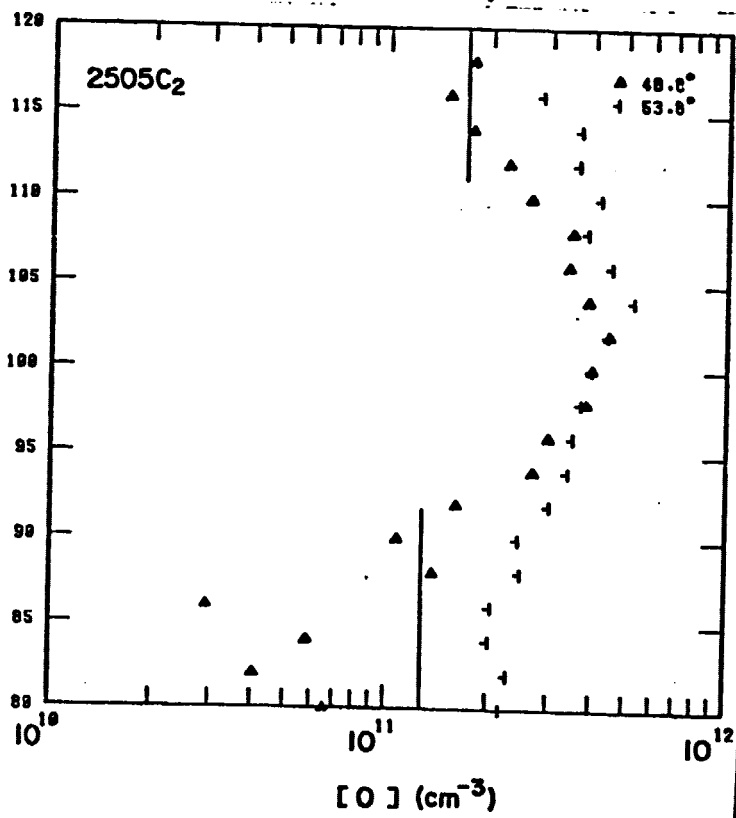
17



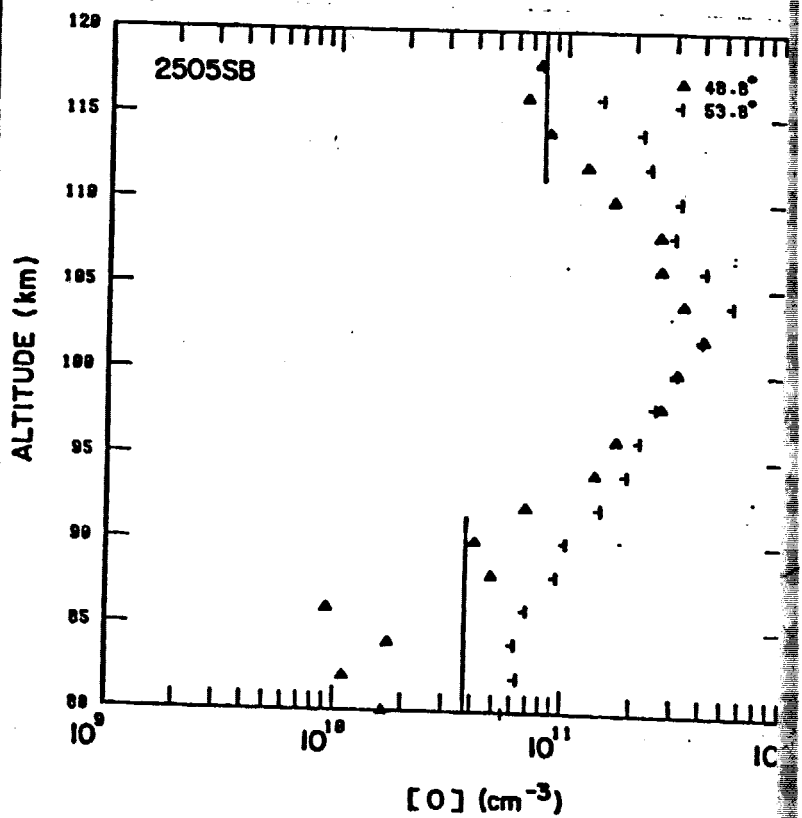
18a



18b



18c



18d

